

FIG. 1

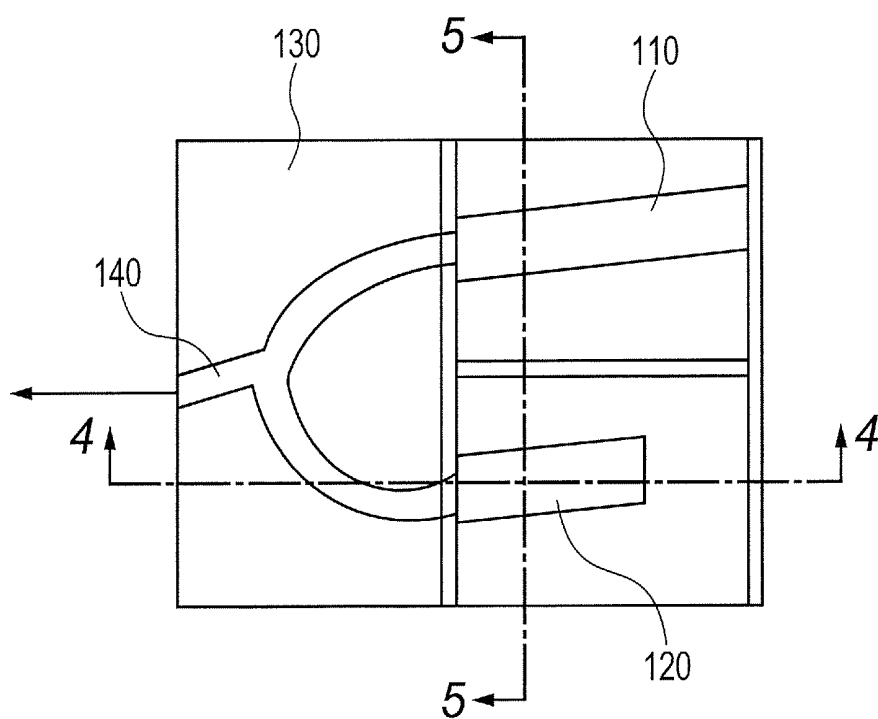


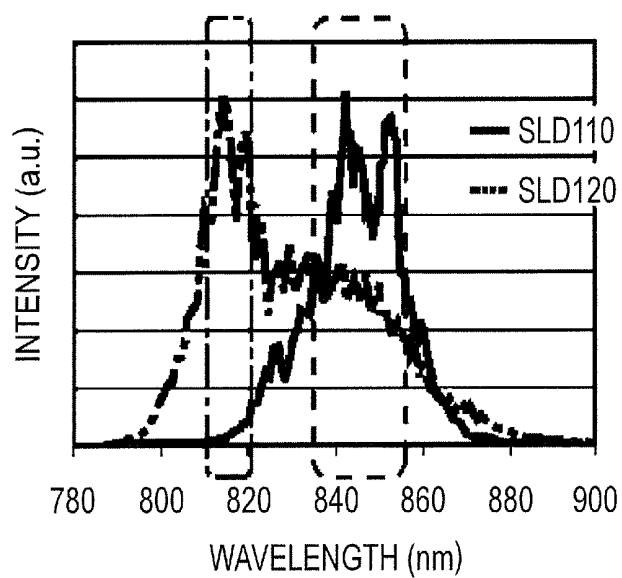
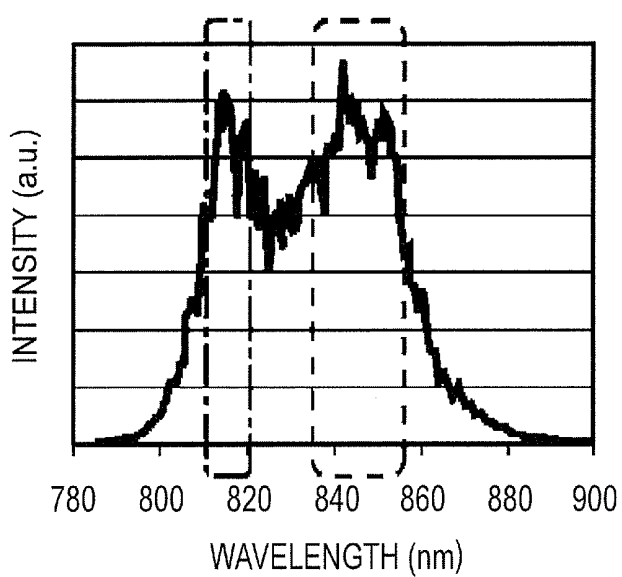
FIG. 2A*FIG. 2B*

FIG. 5

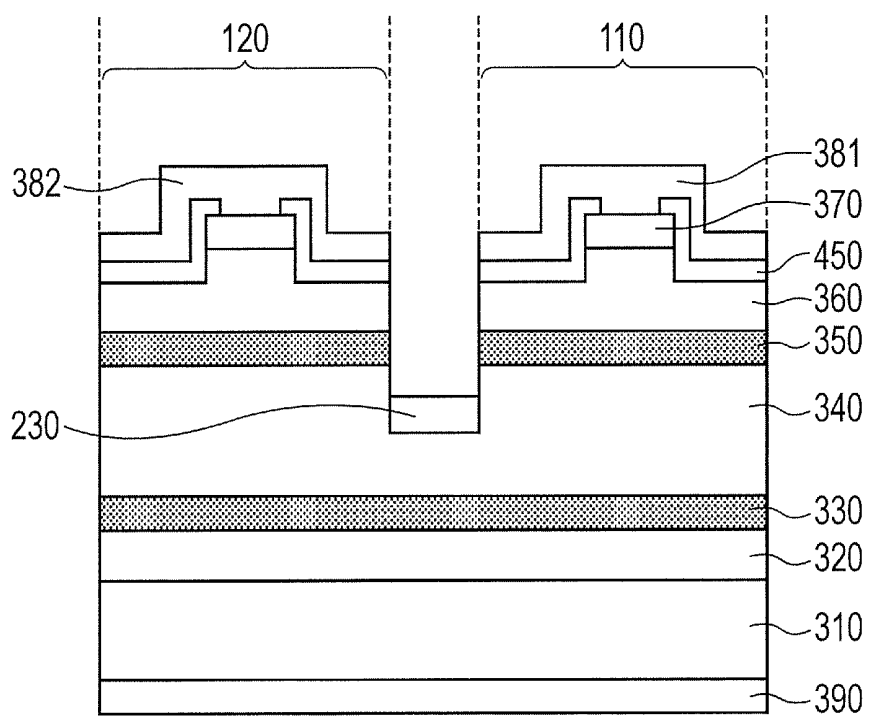


FIG. 6

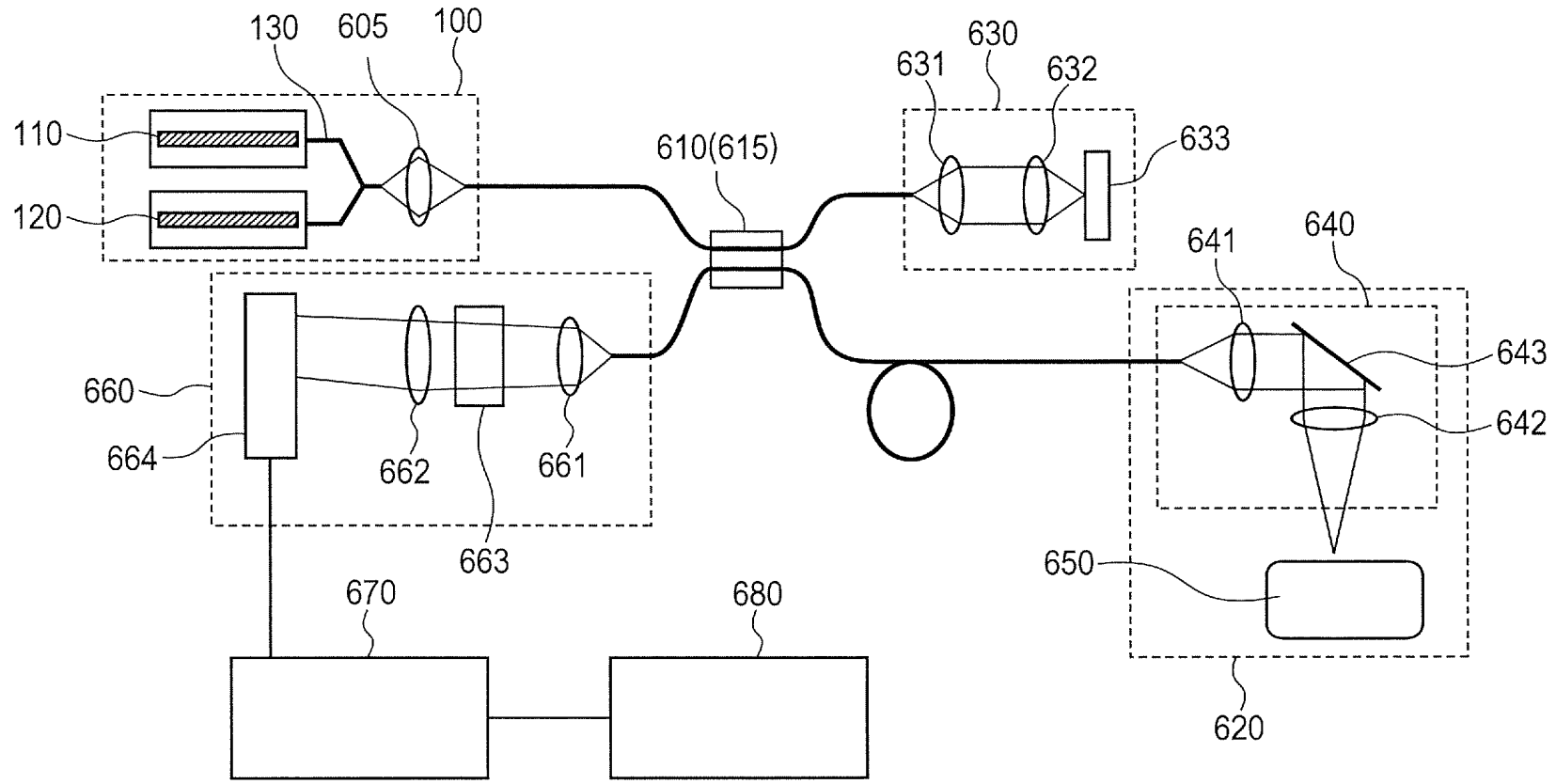


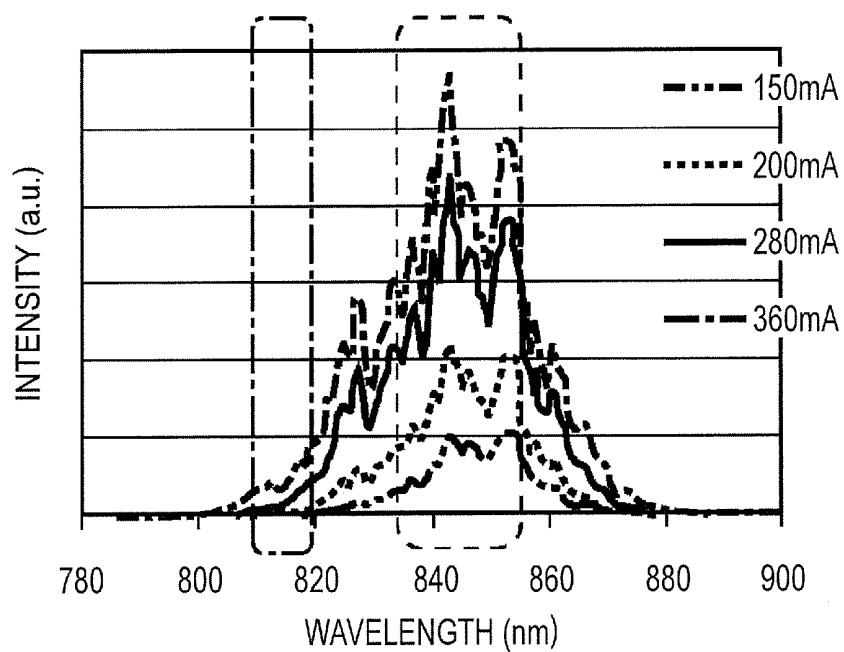
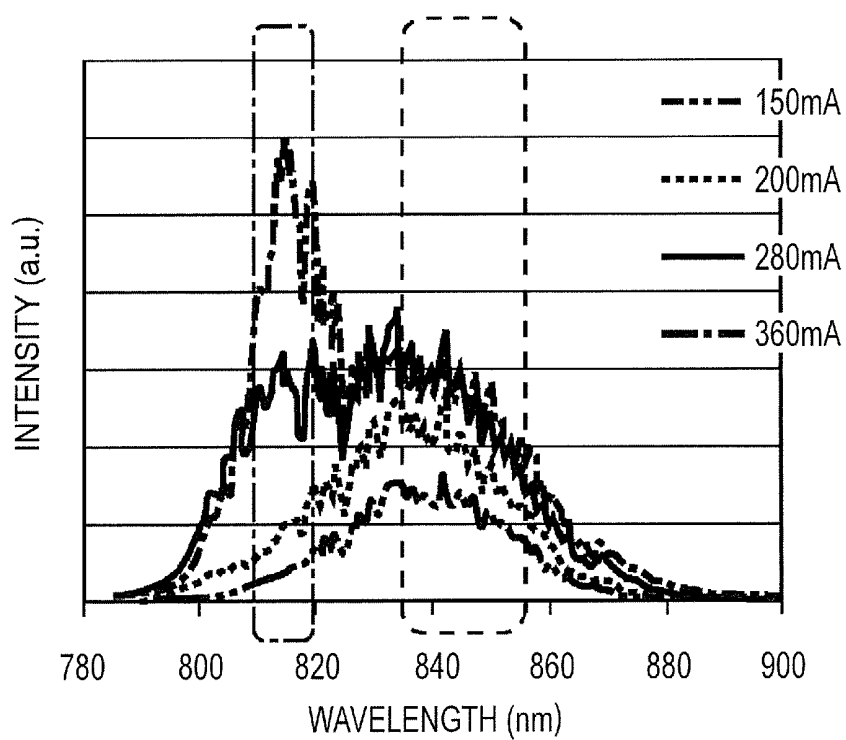
FIG. 7*FIG. 8*

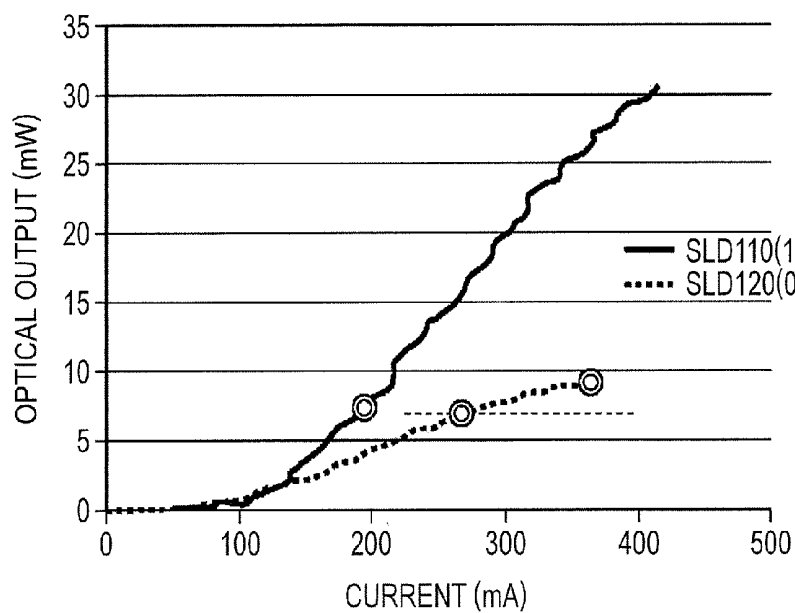
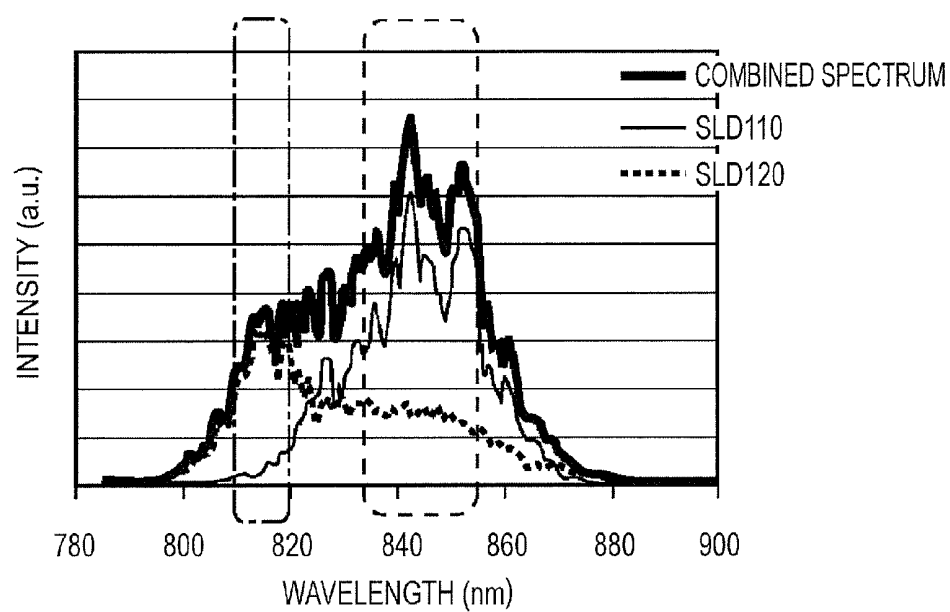
FIG. 9*FIG. 10*

FIG. 11

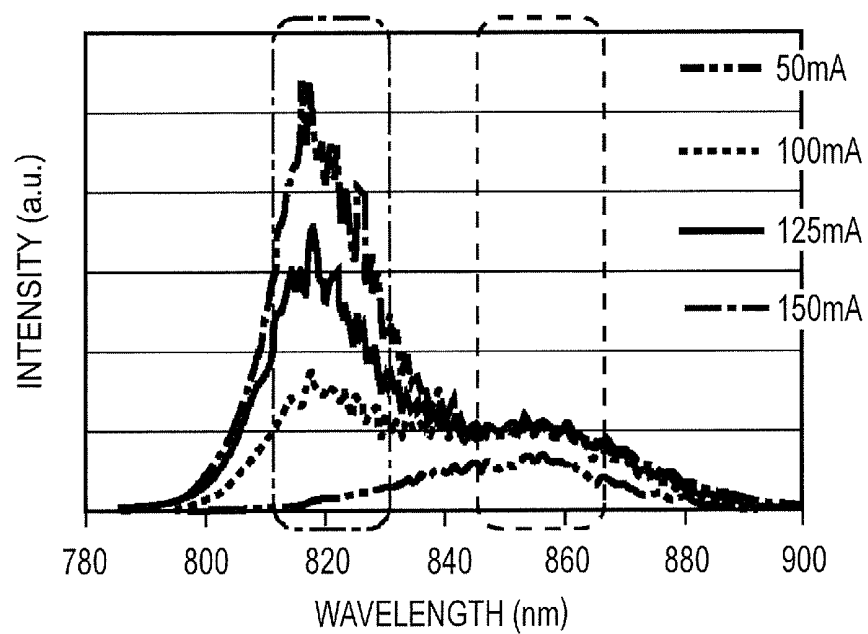


FIG. 12

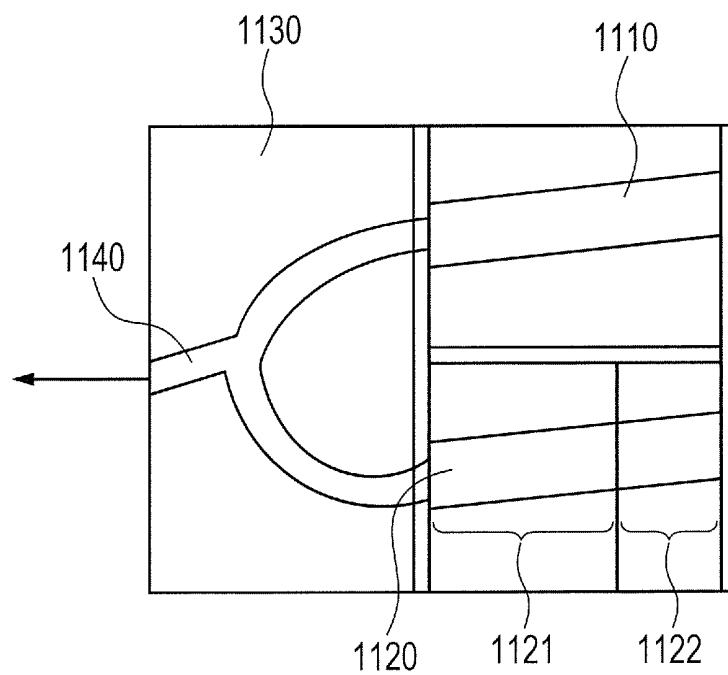


FIG. 13

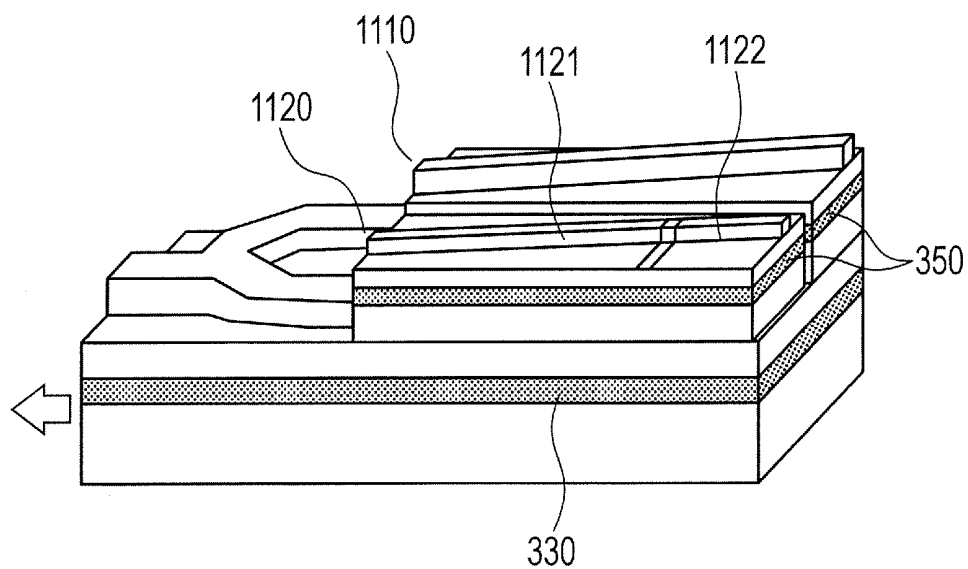
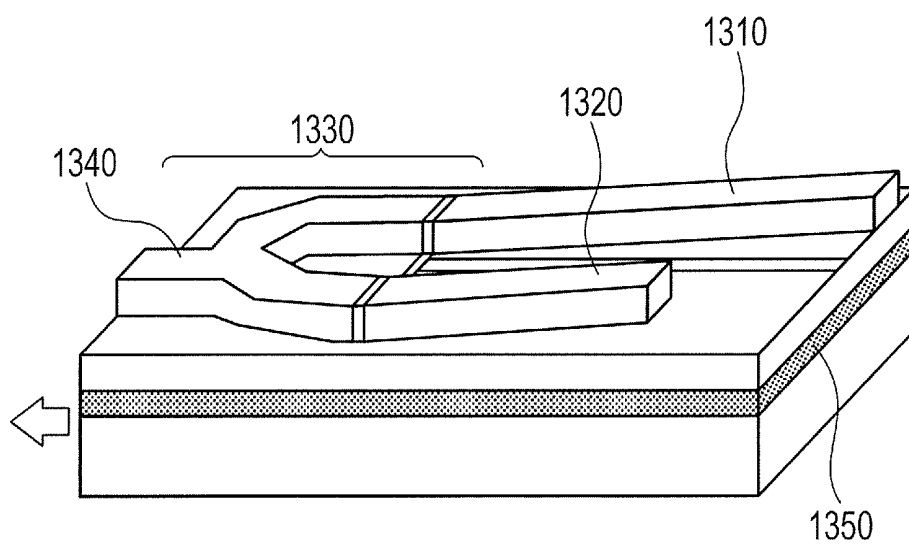


FIG. 14



LIGHT SOURCE DEVICE INCLUDING SUPER LUMINESCENT DIODES, METHOD OF DRIVING THE SAME, AND OPTICAL TOMOGRAPHY IMAGING APPARATUS

BACKGROUND OF THE INVENTION

[0001] 1. Field of the Invention

[0002] The present invention relates to a light source device including super luminescent diodes, a method of driving the light source device, and an optical tomography imaging apparatus.

[0003] 2. Description of the Related Art

[0004] Super luminescent diodes (hereinafter abbreviated as SLDs) are semiconductor light sources that have as broad a spectral distribution as those of light emitting diodes, and are yet capable of producing a relatively large optical output as semiconductor lasers are.

[0005] SLDs, with their characteristics, are attracting attention in the field of medicine and sensing technology where high resolution is demanded, and are used as, for example, the light source of an optical tomography imaging apparatus which utilizes an optical coherence tomography (OCT) system to obtain an optical tomography image of living tissue.

[0006] Broadening the spectrum is necessary in acquiring a high-resolution tomography image. A method of broadening the spectrum in SLDs is described in Quantum Electronics, Vol. 33, No. 6, pp. 471-473, 2003 (hereinafter referred to as Non Patent Literature 1), which uses an active layer having a single quantum well (hereinafter abbreviated as SQW) structure.

[0007] An SLD using SQW accomplishes a full width at half-maximum spectrum that is broad by utilizing the overlapping of emission spectra from two energy levels. In the SLD, attaining a large optical output and attaining a broad full width at half-maximum spectrum are in a trade-off relationship.

[0008] The SLD needs to be driven at a high injection current density in order to achieve a broad full width at half-maximum spectrum by emission spectra from two energy levels, in addition to achieving a large optical output.

[0009] However, when a broad full width at half-maximum spectrum is accomplished in the manner described in Non Patent Literature 1, there is a current density at which two emission peak intensities are equal to each other. Further current injection therefore increases optical output but raises the emission peak intensity of short-wavelength light as well, thereby reducing the full width at half-maximum spectrum.

[0010] In short, the conventional method has a problem in that the device cannot be driven at a certain level of current injection or higher despite the device's ability to produce a larger optical output due to the problem of spectrum characteristics.

SUMMARY OF THE INVENTION

[0011] The present invention has been made in view of the problem described above, and therefore has an object to provide a light source device including super luminescent diodes that are capable of achieving a large optical output as well as a broad spectrum, a method of driving the light source device, and an optical tomography imaging apparatus.

[0012] According to an exemplary embodiment of the present invention, there is provided a light source device,

including at least two super luminescent diodes being a first SLD and a second SLD, which are provided on a same substrate,

[0013] the first SLD and the second SLD including:

[0014] a same active layer having an emission spectrum having multiple peaks;

[0015] a multiplexing portion for multiplexing beams of exit lights which respectively exit from the first SLD and the second SLD; and

[0016] an optical output waveguide for outputting the multiplexed beams,

[0017] the active layer being formed on the same substrate,

[0018] in which the first SLD includes a first electrode portion for driving the first SLD at a first current density, and is structured so that emission peaks on a long wavelength side are dominant, and

[0019] the second SLD includes a second electrode portion for driving the second SLD at a second current density, and is structured so that emission peaks on a short wavelength side are dominant.

[0020] Further, according to an exemplary embodiment of the present invention, there is provided a method of driving a light source device,

[0021] the light source device including at least two super luminescent diodes being a first SLD and a second SLD, which are provided on a same substrate, the first SLD and the second SLD including:

[0022] a same active layer having an emission spectrum having multiple emission peaks;

[0023] a multiplexing portion for multiplexing beams of exit lights which respectively exit from the first SLD and the second SLD; and

[0024] an optical output waveguide for outputting the multiplexed beams,

[0025] the active layer being formed on the same substrate,

[0026] the light source device being configured to output the beams multiplexed in the multiplexing portion from the optical output waveguide,

[0027] the method including:

[0028] driving the first SLD at a first current density at which emission peaks on a long wavelength side of the emission spectrum are dominant; and

[0029] driving the second SLD at a second current density at which emission peaks on a short wavelength side of the emission spectrum are dominant.

[0030] According to the present invention, it is possible to provide a light source device including super luminescent diodes that are capable of achieving a large optical output as well as a broad spectrum, a method of driving the light source device, and an optical tomography imaging apparatus.

[0031] Further features of the present invention will become apparent from the following description of exemplary embodiments with reference to the attached drawings.

BRIEF DESCRIPTION OF THE DRAWINGS

[0032] FIG. 1 is an overhead view illustrating a structural example of a light source device including SLDs according to a first embodiment of the present invention.

[0033] FIG. 2A is a spectrum graph showing the spectra of respective SLDs according to the first embodiment of the present invention.

[0034] FIG. 2B is a spectrum graph in which the spectra of the respective SLDs are combined according to the first embodiment of the present invention.

[0035] FIG. 3 is a perspective view illustrating the structural example of the light source device including SLDs according to the first embodiment of the present invention.

[0036] FIG. 4 is a sectional view taken along the line 4-4 of FIG. 1 to illustrate the layer structure of the light source device including SLDs according to the first embodiment of the present invention.

[0037] FIG. 5 is a sectional view taken along the line 5-5 of FIG. 1 to illustrate the layer structure of the light source device including SLDs according to the first embodiment of the present invention.

[0038] FIG. 6 is a diagram illustrating a structural example of an optical coherence tomography imaging apparatus according to a fourth embodiment which uses a light source device of the present invention.

[0039] FIG. 7 is a spectrum graph of an SLD according to the first embodiment of the present invention.

[0040] FIG. 8 is a spectrum graph of another SLD according to the first embodiment of the present invention.

[0041] FIG. 9 shows current-optical output characteristics of the respective SLDs according to the first embodiment of the present invention.

[0042] FIG. 10 is a spectrum graph showing the spectra of the respective SLDs according to the first embodiment of the present invention, and a spectrum that is obtained by combining the spectra of the SLDs.

[0043] FIG. 11 is a spectrum graph of a spectrum that is observed when an asymmetric quantum well is used in an active layer.

[0044] FIG. 12 is an overhead view illustrating a structural example of a light source device including SLDs according to a second embodiment of the present invention.

[0045] FIG. 13 is a perspective view illustrating the structural example of the light source device including SLDs according to the second embodiment of the present invention.

[0046] FIG. 14 is a perspective view illustrating a structural example of a light source device including SLDs according to a third embodiment of the present invention.

DESCRIPTION OF THE EMBODIMENTS

[0047] The present invention enables a light source device including at least two super luminescent diodes (SLDs) to achieve a large optical output as well as a broad spectrum by setting one of the SLDs so that the emission peaks on the short wavelength side are dominant. A structural example of a light source device including SLDs according to an embodiment of the present invention is described below.

[0048] The light source device including SLDs according to the embodiment of the present invention includes at least two SLDs which are formed on the same substrate and have the same active layer, a multiplexing portion which multiplexes beams of exit lights of the at least two SLDs, and an optical output waveguide for outputting the multiplexed beams.

[0049] In each of the at least two SLDs, the emission spectrum of the active layer has multiple peaks.

[0050] The at least two SLDs include a first SLD which has a first electrode portion for driving the first SLD at a first current density and in which emission peaks on the long wavelength side are dominant, and a second SLD which has a second electrode portion for driving the second SLD at a second current density and in which emission peaks on the short wavelength side are dominant.

[0051] The multiple emission spectrum peaks of the active layer refer to peaks caused by having different energy levels, for example, emission peaks due to the ground level and a high order level, and emission peaks due to different energy levels in a multi-quantum well structure in which the composition or the well width is varied.

[0052] In this type of active layer, what emission peaks are caused varies depending on the SLD structure, the drive current density, and the like.

[0053] Emission peaks on the long wavelength side and emission peaks on the short wavelength side among the multiple peaks as used herein mean emission peaks at long wavelengths where energy is small and emission peaks at short wavelengths where energy is large in each of the SLDs including the first SLD and the second SLD, and do not mean that the wavelengths of the first SLD and the second SLD are long or short relative to each other.

[0054] Although heat may cause each emission peak to deviate by a few nm depending on the current density, emission peaks resulting from the same energy level are treated as the same peak.

[0055] In the second SLD, at least two emission peaks are caused by a second current and, of emission peaks at long wavelengths and emission peaks at short wavelengths, emission peaks at short wavelengths are dominant.

[0056] The second SLD is driven at a high current density so that emission peaks at short wavelengths are dominant. The optical output of the second SLD is therefore larger than that of an SLD driven at an intensity that causes emission peaks at long wavelengths and emission peaks at short wavelengths to be equal to each other. At the same time, the spectrum pattern of the second SLD does not follow the Gaussian curve and the full width at half-maximum spectrum is narrow.

[0057] In the first SLD, on the other hand, a first current is used and emission peaks at long wavelengths are dominant. The first SLD therefore cannot achieve a broad full width at half-maximum spectrum on its own.

[0058] When combined, however, these two SLDs achieve a broad full width at half-maximum spectrum by compensating each other's spectrum patterns which do not follow the Gaussian curve. In addition, with the second SLD where emission peaks at short wavelengths are dominant as an SLD that is larger in optical output than normal, a large optical output is attained as well as a broad spectrum.

[0059] The effect of the present invention is enhanced when a structure is employed that allows fewer emission peaks at short wavelengths in the first SLD than in the second SLD.

[0060] This is because, with the structure suppressing emission peaks at short wavelengths, the current density at which a current is injected can be set high in the compensation of portions of the spectrum of the first SLD where the emission peaks at long wavelengths, and a larger optical output is obtained.

[0061] This structure is realized by, for example, creating a difference between the first SLD and the second SLD with respect to the SLDs' emission regions, or in terms of element length in the optical waveguide direction or optical waveguide width.

[0062] Specifically, setting the element length in the optical waveguide direction larger in the first SLD than in the second SLD suppresses emission peaks at short wavelengths at an even higher current density.

[0063] The reason is that, when the element length is larger, stimulated amplification is more active in an SLD, which increases the rate of carrier consumption and reduces the chance of carrier supply reaching a level that contributes to emission at a short wavelength. Increasing the element length further enables an SLD to produce a larger optical output, and employing an SLD that is larger in element length than the second SLD as the first SLD therefore results in a larger optical output. Embodiments

[0064] Embodiments of the present invention are described below.

First Embodiment

[0065] A structural example of a light source device including SLDs to which the present invention is applied is described as a first embodiment of the present invention with reference to FIGS. 1 and 3.

[0066] The light source device including SLDs of this embodiment includes two SLDs formed on the same substrate, an SLD 110 and an SLD 120, a multiplexing portion 130 for multiplexing beams of light that respectively exit from the SLD 110 and the SLD 120, and an optical output waveguide 140 for outputting the multiplexed light.

[0067] The SLD 110 and the SLD 120 have the same active layer which uses a single quantum well. A barrier layer in this case has a layer structure that enables the single quantum well to emit light on at least the first-order level as well.

[0068] The SLD 110 and the SLD 120 differ from each other in element length in the optical waveguide direction, and the element length of the SLD 110 is larger than that of the SLD 120.

[0069] The SLD 110, the SLD 120, the multiplexing portion 130, and the optical output waveguide 140 use an integrated twin guide structure and a Y-branched waveguide structure 230 to multiplex beams of exit light of the SLD 110 and the SLD 120 and output the light from one output portion.

[0070] The SLD 110 and the SLD 120 employ a ridge waveguide structure.

[0071] The layer structure in the light source device including SLDs of this embodiment is described next.

[0072] FIG. 4 is a sectional view taken along the line 4-4 of FIG. 1 and FIG. 5 is a sectional view taken along the line 5-5 of FIG. 1.

[0073] Some components such as an insulating film are omitted from FIGS. 4 and 5.

[0074] In the layer structure of this embodiment, the following layers are stacked on a substrate.

[0075] That is, stacked on an n-type GaAs substrate 310 are a layer of n-Al_{0.5}GaAs which serves as an n-type cladding layer 320, a layer of Al_{0.2}GaAs which serves as a waveguide layer 330, a layer of n-Al_{0.5}GaAs which serves as an n-type cladding layer 340, a single quantum well of InGaAs which serves as an active layer 350, a layer of p-Al_{0.5}GaAs which serves as a p-type cladding layer 360, and a heavily doped layer of p-GaAs which serves as a contact layer 370.

[0076] After ridge portions 250, the SLDs 110 and 120, and the multiplexing portion 130 are formed, an insulating film 450 and an upper electrode 380 are provided, and a lower electrode 390 is provided under the substrate.

[0077] The upper electrode 380 includes an upper electrode 381 and an upper electrode 382, which respectively drive the SLD 110 and the SLD 120 independently of each other. SiO₂ is used for the insulating film 450, Ti/Au is used for the upper electrode 380, and AuGe/Ni/Au is used for the lower elec-

trode 390. The ridge portions of the SLD 110 and the SLD 120 are partially removed halfway down the p-type cladding layer 360 and the contact layer 370.

[0078] The SLD 110 and the SLD 120 are isolated from each other by etching halfway down the n-type cladding layer 340 which is below the active layer 350.

[0079] The SLD 110 and the SLD 120 which have different element lengths and the Y-branched waveguide 230 are formed by further partial etching that reaches halfway down the n-type cladding layer 340 and leaving the SLD 110, the SLD 120, and the Y-branched waveguide portion.

[0080] The SLD 110 and the SLD 120 have an element length of 1.0 mm and an element length of 0.7 mm, respectively, and both have a ridge width of 4 μm.

[0081] The ridge portions 250 are inclined by 7 degrees with respect to the vertical line of ridge end surfaces and the longitudinal direction of the ridges in order to prevent the reflection at the ridge end surfaces.

[0082] The angle of the Y-branched waveguide 230 in portions that are joined to the SLD 110 and the SLD 120 is inclined at an angle similar to the inclination angle of the SLD 110 and the SLD 120, here, 7 degrees. An output portion of the Y-branched waveguide 230 is also inclined by 7 degrees.

[0083] A multi-layer dielectric film may be added to the output portion of the Y-branched waveguide 230 and end surfaces of the SLD 110 and the SLD 120 in order to control the reflectance.

[0084] A procedure used in this embodiment to create the layers described above is described next.

[0085] First, the layers are formed on the GaAs substrate 310 by growing semiconductor layers sequentially with the use of, for example, metal organic chemical vapor deposition (MOCVD) process in the following manner.

[0086] That is, sequentially grown on the GaAs substrate 310 are the n-type cladding layer 320, the waveguide layer 330, the n-type cladding layer 340, the active layer 350, the p-type cladding layer 360, and the contact layer 370.

[0087] On the wafer where the layers are stacked, the ridge portions 250 are formed by semiconductor lithography process and semiconductor etching process that are common.

[0088] For instance, a dielectric film is formed by sputtering process from, e.g., SiO₂, and then semiconductor lithography process is used to form a stripe forming mask for forming ridges with a photo resist.

[0089] Then dry etching process is used to selectively remove other portions of the semiconductors than the stripe forming mask.

[0090] The removed portions reach halfway down the p-type cladding layer 360 to form the ridged shape that has, for example, a depth of 0.8 μm.

[0091] Next, photolithography process and dry etching process are used to remove the semiconductor layers except the tops of the SLD 110 and the SLD 120.

[0092] The semiconductor layers are etched here halfway down the n-type cladding layer 340, which is between the active layer 350 and the waveguide layer 330, to isolate the SLD 110 and the SLD 120 from each other.

[0093] Photolithography process and dry etching process are used to further remove the semiconductor layers except the SLD 110, the SLD 120, and the Y-branched waveguide 230, and the semiconductor layers are etched halfway down the n-type cladding layer 340 which is between the active layer 350 and the waveguide layer 330.

[0094] The integrated twin guide and the Y-branched waveguide 230 are formed in this manner, and enable the light source device to guide light generated in the SLD 110 and the SLD 120 to an output portion of the optical output waveguide 140.

[0095] Thereafter, the dielectric film 450 is formed on the semiconductor surface from, e.g., SiO₂, and portions of the SiO₂ above the ridge portions 250 are partially removed by photolithography process.

[0096] Next, vacuum evaporation process and lithography process are used to form the upper electrode 380 above each of the SLD 110 and the SLD 120. The upper electrode 380 is, for example, Ti/Au.

[0097] The lower electrode 390 is then formed from, for example, AuGe/Ni/Au. The electrodes and the semiconductors are made into an alloy in a high temperature nitrogen atmosphere in order to obtain the favorable electric characteristics.

[0098] Lastly, crystal surfaces are exposed on the end surfaces by cleaving, and both end surfaces are coated with a dielectric film for adjusting reflectance. The procedure is thus finished.

[0099] A method of driving the light source device including SLDs according to this embodiment is described next.

[0100] The drive currents of the SLD 110 and the SLD 120 are controlled respectively by the upper electrode 381 and the upper electrode 382 independently of each other.

[0101] In the SLD 110 and the SLD 120 where an InGaAs single quantum well is used for the active layer 350, emission peaks at long wavelengths due to the ground level are dominant when the SLDs are driven with the current density set low, and emission peaks at short wavelengths due to the first-order level are dominant when the SLDs are driven with the current density set high.

[0102] Here, in the case where only one emission peak at a long wavelength is recognizable because the intensity of emission peaks at short wavelengths is weak, the one emission peak is called an emission peak at a long wavelength.

[0103] Described first as the characteristics of SLDs that have different element lengths are spectrum characteristics and current-optical output characteristics that are observed when the drive current is varied between the SLD 110 and the SLD 120 (SLD 110: 1.0 mm, SLD 120: 0.7 mm).

[0104] FIG. 7, FIG. 8, and FIG. 9 show the spectrum characteristics of the SLD 110, the spectrum characteristics of the SLD 120, and the current-optical output characteristics, respectively.

[0105] In this case, the emission peak at a long wavelength refers to a peak around 840 nm, and the emission peak at a short wavelength refers to a peak around 810 nm.

[0106] In the SLD 110 which is larger in element length than the SLD 120, emission peaks at long wavelengths are dominant and emission peaks at short wavelengths are suppressed despite a higher current density.

[0107] In the SLD 120, on the other hand, emission peaks at short wavelengths are caused even at a relatively low current density, and emission peaks at long wavelengths and emission peaks at short wavelengths are equal to each other in intensity at a current value of 280 mA, thus forming a Gaussian-like pattern.

[0108] The graph shows that, when the current is increased further, emission peaks at the short wavelengths become dominant at a current value of 360 mA, thereby causing the spectrum pattern to stop following the Gaussian pattern.

[0109] When two SLDs are used in an attempt to broaden the spectrum, the two SLDs are usually given different central wavelengths to compensate each other's wavelength bands and broaden the spectrum.

[0110] In the case of using the same active layer as in this embodiment, optical output is compensated by driving two SLDs 120, which have a broad spectrum, at 280 mA where emission peaks at long wavelengths and emission peaks at short wavelengths are equal to each other in intensity.

[0111] The relationship between optical output and full width at half-maximum spectrum of an SLD is determined by the element length of the SLD and, as the element length becomes larger, the optical output becomes larger but the full width at half-maximum spectrum becomes narrower.

[0112] Consequently, when all the SLDs used are the SLDs 120 which have a short element length, optical output is reduced as much as the full width at half-maximum spectrum is broadened.

[0113] In the case where the only SLDs used are the SLDs 110 which have a large element length and are large in optical output, on the other hand, the full width at half-maximum spectrum is narrower as shown in FIGS. 7 and 9.

[0114] This embodiment is structured so as to remedy these drawbacks, and sets a higher current density for the SLD 120 which has a small optical output and thus increases the optical output by driving the SLD 120 in a manner that causes emission peaks at short wavelengths to be dominant.

[0115] The SLD 120 is driven in combination with the SLD 110 which is large in optical output and in element length, to thereby balance spectrum broadening and optical output increase.

[0116] Specifically, the SLD 110 is driven at 200 mA and the SLD 120 is driven at 360 mA in this embodiment.

[0117] In other words, the SLDs 110 and 120 are driven so that emission peaks at long wavelengths are dominant in the SLD 110 whereas emission peaks at short wavelengths are dominant in the SLD 120.

[0118] The spectra of the SLD 110 and the SLD 120 driven in this manner are shown in FIG. 2A, and a combined spectrum of the SLD 110 and the SLD 120 is shown in FIG. 2B.

[0119] The graphs confirm that combining the spectra of the SLD 110 and the SLD 120 yields a broad spectrum pattern in which emission peaks at short wavelengths and emission peaks at long wavelengths are substantially equal to each other in intensity.

[0120] As shown in FIG. 9, the optical output of the SLD 120 driven at 360 mA increases to 9.0 mW from 7.5 mW, which is the optical output of the SLD 120 driven at a current of 280 mA, which is usually used in spectrum broadening and at which emission peaks at long wavelengths and emission peaks at short wavelengths are equal to each other in intensity.

[0121] An additional optical output of 8 mW is obtained by driving the SLD 110, which is larger in optical output and has fewer emission peaks at short wavelengths than the SLD 120, at 200 mA, which brings the total optical output to 17 mW.

[0122] Compared to the case where two SLDs 120 driven at a current of 280 mA are placed side by side, a larger optical output is thus attained while accomplishing an equally broad spectrum.

[0123] To increase the optical output even more, the SLD 110 and the SLD 120 can be driven at, for example, 280 mA and 360 mA, respectively. The total optical output obtained in this case is 25 mW. The intensity of emission peaks at long wavelengths in this example is higher than that of emission

peaks at short wavelengths as shown in FIG. 10, but a larger optical output than under the condition described above can be obtained.

[0124] A spectrum pattern and an optical output that are suitable for a specific use can be obtained by varying the drive condition in this manner.

[0125] To vary the drive condition while avoiding changing the full width at half-maximum spectrum too much, it is required that the difference between the sum of the emission peak intensities of the two SLDs at short wavelengths and the sum of the emission peak intensities of the two SLDs at long wavelengths not be twice or more.

[0126] In other words, the relationship " $\frac{1}{2}A < B < 2A$ " needs to be satisfied, where "A" represents the sum of intensities of the emission peaks of the first SLD and the second SLD on the short wavelength side, and "B" represents the sum of intensities of the emission peaks of the first SLD and the second SLD on the long wavelength side.

[0127] In addition to the drive condition, the element lengths of the SLDs may be changed to suit individual cases, and these may be combined under an appropriate condition to obtain an arbitrary spectrum pattern and optical output.

[0128] The present invention is not limited to the forming method, the semiconductor materials, the electrode materials, the dielectric materials, and the like that are disclosed in the embodiment of the present invention, and other methods and materials can be used as long as the choice does not depart from the spirit of the present invention.

[0129] For instance, the substrate used may be a p-type GaAs substrate and, in this case, the conductivity types of the semiconductor layers are changed accordingly.

[0130] The active layer which uses a single quantum well here may instead use, for example, a multi-quantum well or an asymmetric multi-quantum well in which the well width and the composition ratio are varied.

[0131] In that case, an emission peak at a short wavelength may be of light emission due to the first-order level whereas an emission peak at a long wavelength is of light emission due to the ground level as in the case where a single quantum well is used.

[0132] Alternatively, because each quantum well structure is different, emission peaks due to different energy levels that correspond to the different quantum well structures may be treated as an emission peak at a short wavelength and an emission peak at a long wavelength.

[0133] For instance, when the active layer uses an asymmetric multi-quantum well formed from different well layer materials, specifically, InGaAs, GaAs, and AlGaAs, spectrum characteristics of FIG. 11 are observed.

[0134] Emission peaks at long wavelengths which are dominant when the drive current density is low are peaks around 860 nm, and emission peaks at short wavelengths which are dominant when the drive current density is high are peaks around 820 nm. Raising the current density increases the intensity of emission peaks at short wavelengths twice or more the intensity of emission peaks at long wavelengths. In the case of an active layer having such a spectrum, there is a large difference from an optical output produced when the active layer is driven with a drive current at which emission peaks at long wavelengths and emission peaks at short wavelengths are equal to each other in intensity, and the effect of applying the present invention is enhanced.

[0135] The materials are also not limited to those given above, and light emitting materials such as GaAs, GaInP, AlGaInN, AlGaInAsP, and AlGaAsSb may be used.

[0136] The ridge width is not limited to 4 μm and may be changed to suit individual cases.

[0137] This embodiment employs an SLD structure in which a ridge portion is used for each SLD and the ridges are inclined. However, any structure that operates as an SLD can be employed, for example, a structure that prevents reflection with a window structure instead of an inclined ridge.

[0138] The multiplexing portion is not limited to the Y-branched multiplexer employed here, and other multiplexers that have a multiplexing function such as a multi-mode interference (MMI) multiplexer may be used.

[0139] The SLD 110, the SLD 120, and the multiplexing portion 130 here are built monolithically. The structure of this embodiment may instead be accomplished by building only the SLD 110 and the SLD 120 monolithically and multiplexing beams of light from the SLDs 110 and 120 with a fiber coupler or the like in the multiplexing portion 130.

[0140] This embodiment, which uses two SLDs, may also be structured so that beams of light from three or more SLDs are multiplexed.

[0141] In this case, every SLD may have a different element length, or, to compensate the emission peaks at short wavelengths more, the element length may be determined so that, for example, two SLDs are given two different short element lengths while one SLD is given a large element length.

Second Embodiment

[0142] A structural example in which two SLDs, an SLD 1110 and an SLD 1120, have the same element length is described as a second embodiment of the present invention.

[0143] The SLD 1120 has an upper electrode that is divided into two in the optical waveguide direction.

[0144] The structure of this embodiment is described with reference to an overhead view of FIG. 12 and a perspective view of FIG. 13. A light source device of this embodiment includes a multiplexing portion and an optical output waveguide for outputting the multiplexed light.

[0145] Specifically, as in the first embodiment, the light source device includes two SLDs formed on the same substrate, the SLD 1110 and the SLD 1120, a multiplexing portion 1130 for multiplexing beams of light that respectively exit from the SLD 1110 and the SLD 1120, and an optical output waveguide 1140 for outputting the multiplexed light. The SLD 1110 and the SLD 1120 have the same active layer 350.

[0146] The two divided pieces of electrode create different current injection regions, a region 1121 and a region 1122, in the SLD 1120.

[0147] Ti/Au of the upper electrode and a GaAs contact layer are removed by, for example, photolithography process and wet etching process from a region between the region 1121 and the region 1122, thereby forming the region 1121 and the region 1122 into separate current injection regions.

[0148] Here, the element length of the SLD 1110 and the SLD 1120 is 1.0 mm, and the lengths of the regions 1121 and 1122 of the SLD 1120 are 0.7 mm and 0.3 mm, respectively, in the optical waveguide direction. The distance between the region 1121 and the region 1122 is a few μm .

[0149] How the SLD 1110 and the SLD 1120 are driven in this embodiment is described next.

[0150] In the SLD 1120, a current is injected to the region 1121 in a normal manner and no current a weak current is injected to the region 1121.

[0151] Then, the region 1122 of the SLD 1120 works as an absorption region despite the fact that the SLD 1110 and the SLD 1120 have the same element length. The substantial emission region of the SLD 1120 is therefore the region 1121, and the effect of varying the element length in the manner of the first embodiment is obtained.

[0152] In other words, the SLD 1110 can be considered as an SLD that has a larger element length than the SLD 1120. Driving the SLD 1110 and the region 1121 of the SLD 1120 in the manner of the first embodiment therefore yields a broad spectrum and a large optical output.

[0153] Employing this structure allows the use of a cleaved surface in both the SLD 1110 and the SLD 1120, which leads to the stabilizing of characteristics.

[0154] The SLD 1120 alone is divided into two different current injection regions here. Alternatively, the SLD 1120 may be divided into three or more regions, or the SLD 1110 may be divided into multiple regions as well.

[0155] In this case, the spectrum pattern can be controlled more arbitrarily by varying the amount of current injection from one region to another. Dividing each SLD into multiple current injection regions in this manner may be applied to the first embodiment.

[0156] The ridge width may be varied between the SLD 1110 and the SLD 1120 which have the same element length to control the current density and drive the SLDs 1110 and 1120 in a manner that causes emission peaks at long wavelengths to be dominant in the SLD 1110 and emission peaks at short wavelengths to be dominant in the SLD 1120.

[0157] The ridge width may be varied by, for example, in addition to simply varying the widths of the SLD 1110 and the SLD 1120, employing a tapered structure in which the ridge in each SLD becomes narrower toward the multiplexing portion along the optical waveguide direction.

Third Embodiment

[0158] The following structural example is described as a third embodiment of the present invention with reference to FIG. 14.

[0159] That is, this embodiment employs a structure in which two SLDs, an SLD 1310 and an SLD 1320, a multiplexing portion 1330 for multiplexing beams of light that respectively exit from the SLD 1310 and the SLD 1320, and an optical output waveguide 1340 for outputting the multiplexed light are all formed on the same substrate and have the same active layer 1350.

[0160] As illustrated in FIG. 14, this embodiment is structured so that an n-type cladding layer, an active layer, a p-type cladding layer, and a contact layer are stacked on an n-type substrate.

[0161] Ridge portions of the SLD 1310 and the SLD 1320, the multiplexing portion 1330, and the optical output waveguide 1340 are formed by semiconductor lithography process and semiconductor etching process that are common. An upper electrode is formed on each of the SLD 1310, the SLD 1320, and the multiplexing portion 1330 so that the three can be driven with a current independently of one another.

[0162] Ti/Au of the upper electrodes and a GaAs contact layer are removed by, for example, photolithography process and wet etching process from a region between the SLD 1310 and the multiplexing portion 1330 and from a region between

the SLD 1320 and the multiplexing portion 1330, thereby electrically isolating one from the other.

[0163] In this embodiment in which an electrode is formed above the multiplexing portion 1330 in addition to electrodes above the SLD 1310 and the SLD 1320, a current can be injected to the multiplexing portion 1330 as well.

[0164] Injecting a current to the multiplexing portion 1330 and the optical output waveguide 1340 at some current density prevents the absorption of guided light in the multiplexing portion 1330 and the optical output waveguide 1340.

Fourth Embodiment

[0165] A structural example of an OCT apparatus (optical tomography imaging apparatus) including a light source device of the present invention is described as a fourth embodiment of the present invention with reference to FIG. 6.

[0166] As illustrated in FIG. 6, the OCT apparatus of this embodiment includes an optical output portion 100, a light splitting portion 610 for splitting the light that exits from the optical output portion 100 into reference light and measurement light, and a reference light reflecting portion 630.

[0167] The OCT apparatus also includes a measuring portion 620 which includes a measurement object 650 and an irradiation optical system 640 for irradiating the measurement object 650 with light to guide the reflected light thereof, and an interfering portion 615 for causing interference between the measurement light that has been reflected and the reference light that has been reflected by a reference mirror which constitutes a reference portion.

[0168] The OCT apparatus further includes a light detecting portion 660 which detects the interfering light provided by the interfering portion, an image processing portion 670 which executes the image processing (obtains a tomography image) based on the light detected by the light detecting portion 660, and an image output monitor portion 680.

[0169] A specific structure of the OCT apparatus is described below.

[0170] The optical output portion 100 includes the SLD 110 and the SLD 120, the multiplexing portion 130 which couples two beams of exit light, and a lens 605 which couples light to an optical fiber.

[0171] Light enters the light splitting portion 610 via an optical fiber to be demultiplexed into reference light and measurement light, and a part of the demultiplexed light enters the reference light reflecting portion 630.

[0172] Here, the same fiber coupler is used as the light splitting portion 610 and the interfering portion 615.

[0173] The reference light reflecting portion 630 includes collimator lenses 631 and 632 and a reflecting mirror 633. Light is reflected by the reflecting mirror 633 to enter the optical fiber again.

[0174] The measurement light which is the other beam of light created by the demultiplexing of light from the optical fiber in the light splitting portion 610 enters the measuring portion 620.

[0175] The irradiation optical system 640 of the measuring portion 620 includes collimator lenses 641 and 642 and a reflecting mirror 643 for bending a light path by 90°. The irradiation optical system 640 has a role of causing the incident light to irradiate the measurement object 650 and coupling the incident light that is reflected by the measurement object 650 to the optical fiber again.

[0176] The beams of light returning from the reference light reflecting portion 630 and the measuring portion 620

pass through the interfering portion 615 and enter the light detecting portion 660. The light detecting portion 660 includes collimator lenses 661 and 662, a spectroscopy 663, and a line sensor 664 for obtaining the spectrum information of light that is dispersed by the spectroscopy 663. The spectroscopy 663 uses a grating.

[0177] The light detecting portion 660 is structured to obtain the spectrum information of light entering the light detecting portion 660. The information obtained by the light detecting portion 660 is converted into an image by the image processing portion 670 which executes conversion to a tomography image. Tomography image information which is the final output is thus obtained. The tomography image information is displayed as a tomography image on the image output monitor portion 680 which includes a display screen of a personal computer or the like.

[0178] The feature of this embodiment is the optical output portion 100 which is capable of producing a large optical output of a broad spectrum when a light source device including SLDs of the present invention is used. Tomography image information that is high in depth resolution can therefore be obtained.

[0179] This OCT apparatus is useful for tomography imaging in the practices of ophthalmology, dentistry, dermatology, and the like.

[0180] While the present invention has been described with reference to exemplary embodiments, it is to be understood that the invention is not limited to the disclosed exemplary embodiments. The scope of the following claims is to be accorded the broadest interpretation so as to encompass all such modifications and equivalent structures and functions.

[0181] This application claims the benefit of Japanese Patent Application No. 2012-061491, filed Mar. 19, 2012, which is hereby incorporated by reference herein in its entirety.

What is claimed is:

1. A light source device, comprising at least two super luminescent diodes being a first SLD and a second SLD, which are provided on a same substrate,

the first SLD and the second SLD comprising:

a same active layer having an emission spectrum having multiple peaks;

a multiplexing portion for multiplexing beams of exit lights which respectively exit from the first SLD and the second SLD; and

an optical output waveguide for outputting the multiplexed beams,

the active layer being formed on the same substrate,

wherein the first SLD comprises a first electrode portion for driving the first SLD at a first current density, and is structured so that emission peaks on a long wavelength side are dominant, and

the second SLD comprises a second electrode portion for driving the second SLD at a second current density, and is structured so that emission peaks on a short wavelength side are dominant.

2. The light source device according to claim 1, wherein the first SLD has a larger element length in an optical waveguide direction than an element length of the second SLD in the optical waveguide direction.

3. The light source device according to claim 1, wherein the first current density is lower than the second current density.

4. The light source device according to claim 1, wherein the active layer comprises a single quantum well.

5. The light source device according to claim 4, wherein emission due to a ground level is dominant among the emission peaks on the long wavelength side, and emission due to a first-order level is dominant among the emission peaks on the short wavelength side.

6. The light source device according to claim 1, wherein the first SLD and the second SLD have a same element length in an optical waveguide direction.

7. The light source device according to claim 1, wherein at least one of the first SLD and the second SLD comprises an electrode that is divided into at least two pieces in the optical waveguide direction.

8. The light source device according to claim 1, wherein, in the second SLD, the emission peaks on the short wavelength side at the second current density have a peak intensity twice or more higher than a peak intensity of the emission peaks on the long wavelength side.

9. The light source device according to claim 1, wherein the multiplexing portion and the optical output waveguide are formed monolithically with at least the two super luminescent diodes.

10. The light source device according to claim 9, wherein the multiplexing portion and the optical output waveguide have the same active layer as the active layer of the first SLD and the second SLD.

11. The light source device according to claim 1, wherein the multiplexing portion comprises an electrode.

12. A method of driving a light source device,

the light source device comprising at least two super luminescent diodes being a first SLD and a second SLD, which are provided on a same substrate, the first SLD and the second SLD comprising:

a same active layer having an emission spectrum having multiple emission peaks;

a multiplexing portion for multiplexing beams of exit lights which respectively exit from the first SLD and the second SLD; and

an optical output waveguide for outputting the multiplexed beams,

the active layer being formed on the same substrate,

the light source device being configured to output the beams multiplexed in the multiplexing portion from the optical output waveguide,

the method comprising:

driving the first SLD at a first current density at which emission peaks on a long wavelength side of the emission spectrum are dominant; and

driving the second SLD at a second current density at which emission peaks on a short wavelength side of the emission spectrum are dominant.

13. The method of driving a light source device according to claim 12,

wherein at least one of the first SLD and the second SLD comprises an electrode that is divided into at least two pieces in an optical waveguide direction, and

the first SLD and the second SLD are driven at current densities that are set independently of each other.

14. The method of driving a light source device according to claim 12, wherein, in an emission spectrum resulting from driving the first SLD at the first current density and an emission spectrum resulting from driving the second SLD at the second current density, the following relationship is satisfied: $\frac{1}{2}A < B < 2A$

where “A” represents a sum of intensities of the emission peaks of the first SLD and the second SLD on the short wavelength side, and “B” represents a sum of intensities of the emission peaks of the first SLD and the second SLD on the long wavelength side.

15. An optical tomography imaging apparatus, comprising:
the light source device according to claim 1;

a measuring portion which irradiates a measurement object with light from the light source device to guide the light reflected from the measurement object;

a reference portion which irradiates a reference mirror with light from the light source device to guide the light reflected from the reference mirror;

an interfering portion which causes interference between the light reflected from the measuring portion and the light reflected from the reference portion;

a light detecting portion which detects interfering light from the interfering portion; and

an image processing portion which obtains a tomography image of the measurement object based on the interfering light detected by the light detecting portion.

* * * * *



US 20090039235A1

(19) **United States**(12) **Patent Application Publication**
MacFarlane et al.(10) **Pub. No.: US 2009/0039235 A1**(43) **Pub. Date: Feb. 12, 2009**(54) **METHOD FOR DETERMINING LOCATION
AND MOVEMENT OF A MOVING OBJECT****Related U.S. Application Data**(63) Continuation-in-part of application No. 11/282,046,
filed on Nov. 16, 2005.(76) Inventors: **Duncan L. MacFarlane**, Dallas,
TX (US); **Richard Briggs**, Dallas,
TX (US); **Andrei A. Zaremba**,
Richardson, TX (US); **Keith D.**
White, Gainesville, FL (US)**Publication Classification**(51) **Int. Cl.**
G01B 11/00 (2006.01)
G01R 33/28 (2006.01)
(52) **U.S. Cl.** **250/206.1; 324/318**(57) **ABSTRACT**

The present invention discloses a method for determining location and movement of a moving object. One embodiment of the method tracks the movement of a target during medical imaging scanning and transmits the position shift to the medical imaging scanning device in real time. The method includes the steps of projecting structured light on the target, receiving the reflection of structured light, converting the received structured light into spatial positions, and transmitting the positional shift to the medical imaging scanning device. The method further includes the step of adjusting the medical imaging scanning device in response to the positional change to increase accuracy.

Correspondence Address:

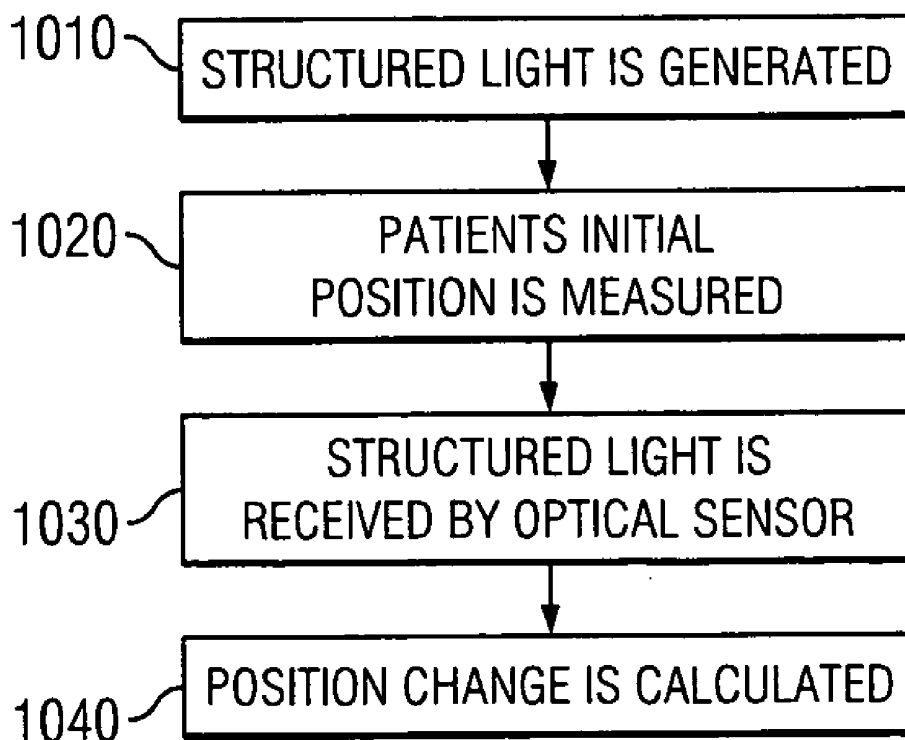
George R. Schultz**Schultz & Associates, P.C.****One Lincoln Centre, 5400 LBJ Freeway, Suite1200**
Dallas, TX 75240 (US)(21) Appl. No.: **12/152,917**(22) Filed: **May 19, 2008**

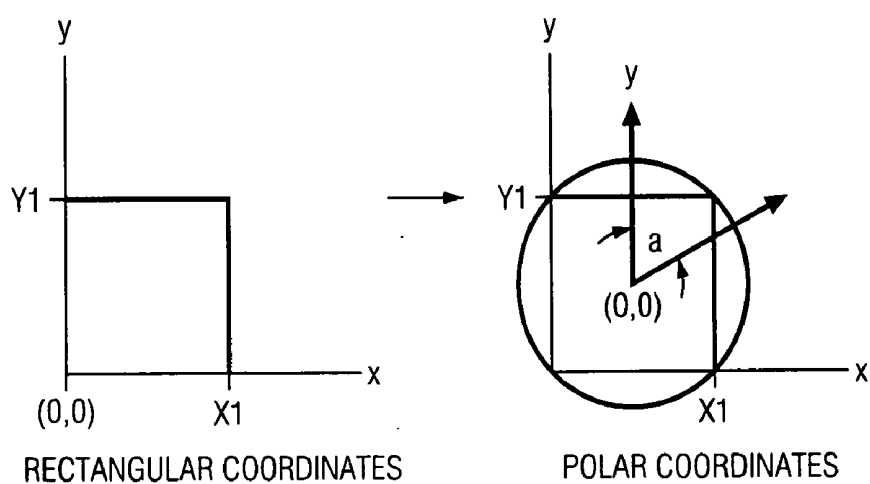
FIG. 1

```
%CALCULATIONS OF THE FIRST MATRIX
A=0; B=0; C=0; D=0;
c=sum(t);      %sum of the columns
r=sum(t');     %sum of the rows
For j=1:40,
A=A+c(j)*j;    %calculating the weighed average for the columns
end
for i=1:40,
B=B+r(i)*i;    %calculating the weighed average for the rows
end
for j=1:40,
C=C+c(j);      %calculating the sum of the vector c(columns);
end
for i=1:40,
D=D+r(i);      %calculating the sum of the vector r(rows);
end
A=A/C;         %A=center of mass of rows of the matrix
B=B/D;         %B=center of mass of the columns on the matrix

%CALCULATIONS FOR THE SECOND MATRIX
Q=0; W=0; E=0; R=0;
c1=sum(y);     %sum of the columns
r1=sum(y');    %sum of the rows
for jj=1:40,
Q=Q+c1(jj)*jj; %calculating the weighted average for the columns
end
for jj=1:40,
E=E+c1(jj);    %calculating the sum of the vector c1 (columns);
end
for ii=1:40,
R=R+r1(ii);    %calculating the sum of the vector r1 (rows);
end
Q=Q/E; %Q=center of mass of rows of the matrix
W=W/R;  %W=center of mass of the columns on the matrix
%Calculation of the distance between the two
%Our variables are A->Q;B->W;
columns=abs(A-Q);
rows=abs(B-W);
distance=(rows^2+columns^2)^.5;
angle=atan(columns/rows);
```

FIG. 2

```
x=imread('zero.jpg');  
y=imread('Image_0140.jpg');  
c=normxcorr2(x(:,1), y(:,1));  
[max_c, imax]=max(abs(c(:)));  
[ypeak, xpeak]=ind2sub(size(c),  
imax(1));  
XY_offset=[(xpeak-size(y,2))  
(ypeak-size(y,1))];
```

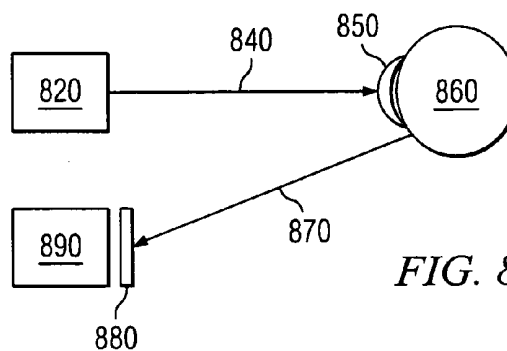
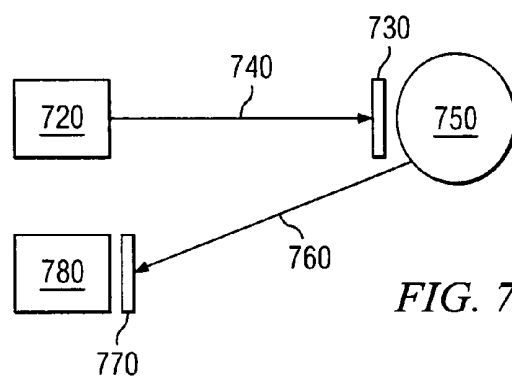
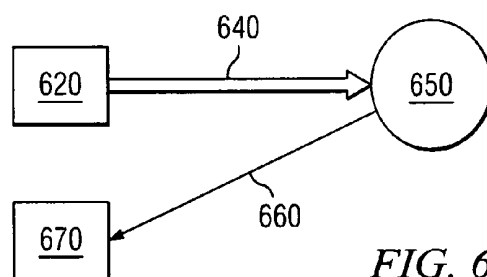
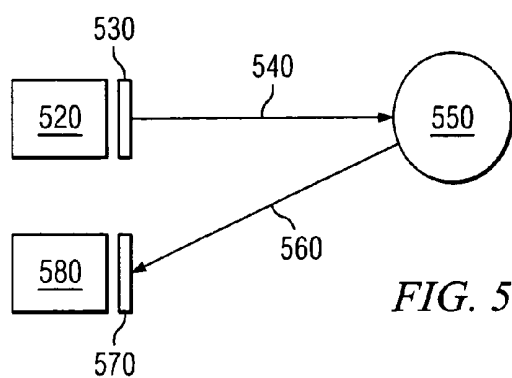
*FIG. 3*

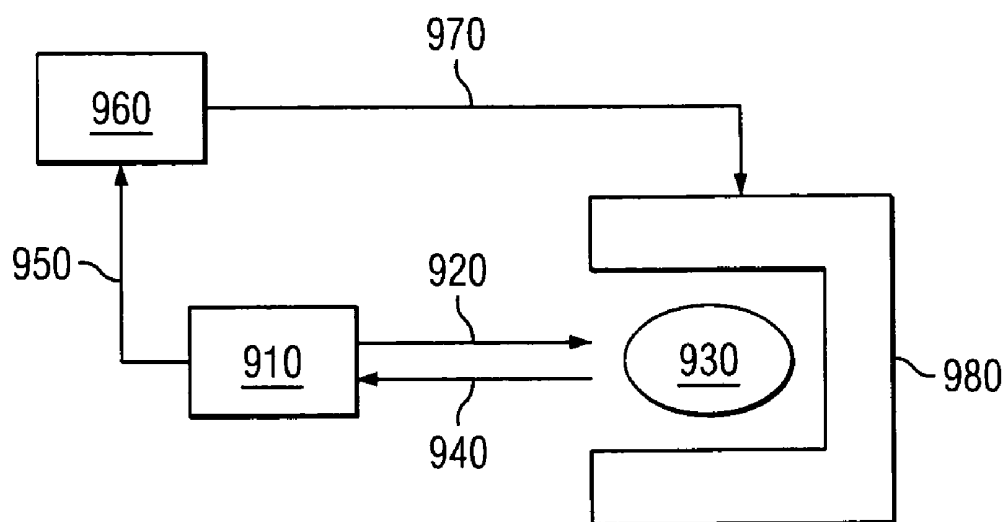
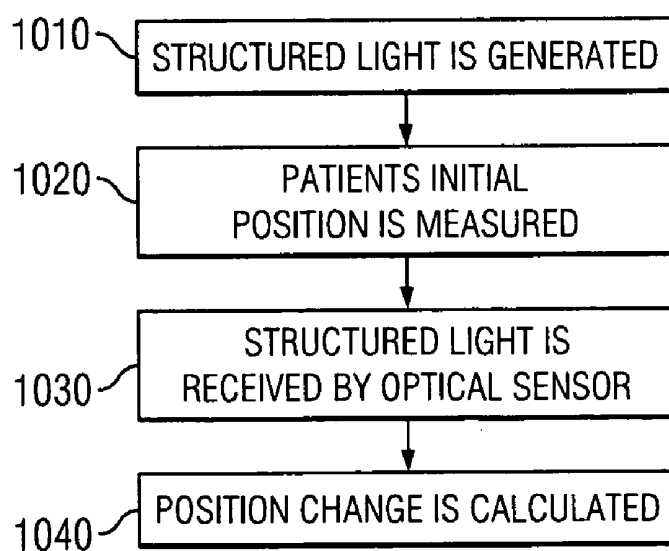
```

in1=imread('rect1.jpg'); %input1=abs(fft2(in1)); input1=imread('rect1.jpg');
%input1=double(input1(:,:));
oRows=size(input1,1);
oCols=size(input1,2);
dTheta=2*pi/oCols; % the step size for theta
b=10 A (log10(oRows)/oCols); % base for the log-polar conversion
for i=1:oRows % rows
    for j=1:oCols % columns
        r=b ^ i-1; % the log-polar
        theta=j*dTheta;
        x=round(r*cos(theta)+size(input1,2)/2);
        y=round(r*sin(theta)+size(input1,1)/2);
        if (x>0) & (y>0) & (x<size(input1,2)) & (y<size(input1,1))
            output1(i,j)=input1(y,x);
        end
    end
end
in2=imread('rect2.jpg'); input2=in2; %input2=double(input2(:,:));
%input2=abs(fft2(in2rotated));
oRows=size(input2,1); oCols=size(input2,2);
dTheta=2*pi/oCols; % the step size for theta
b=10 A (log10(oRows)/oCols); % base for the log-polar conversion
for i=1:oRows % rows
    for j=1:oCols % columns
        r=b ^ i-1; % the log-polar
        theta=j*dTheta;
        x=round(r*cos(theta)+size(input2,2)/2);
        y=round(r*sin(theta)+size(input2,1)/2);
        if (x>0) & (y>0) & (x<size(input2,2)) & (y<size(input2,1))
            output2(i,j)=input2(y,x);
        end
    end
end;
x=output1; y=output2; fx=(fft2(output1)); fy=(fft2(output2));
%fx=fftshift(fx); %fy=fftshift(fy); %polar(fx); %figure,polar(fy);
c=normxcorr2(fx(:,:),fy(:,:));
[max_c,imax]=max(abs(c(:)));
[ypeak,xpeak]=ind2sub(size(c),imax(1));
XY_offset=[(xpeak-size(y,2)) (ypeak-size(y,1))]; %imagesc(output1), colormap('gray'),
figure, imagesc(output2), colormap('gray');

```

FIG. 4



*FIG. 9**FIG. 10*

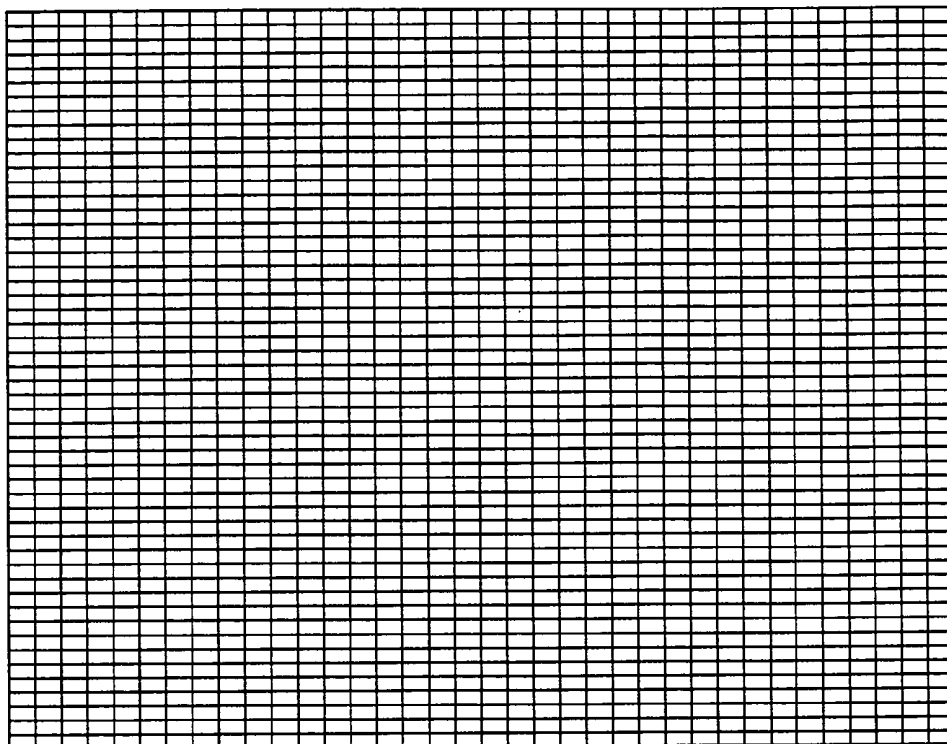


FIG. 11

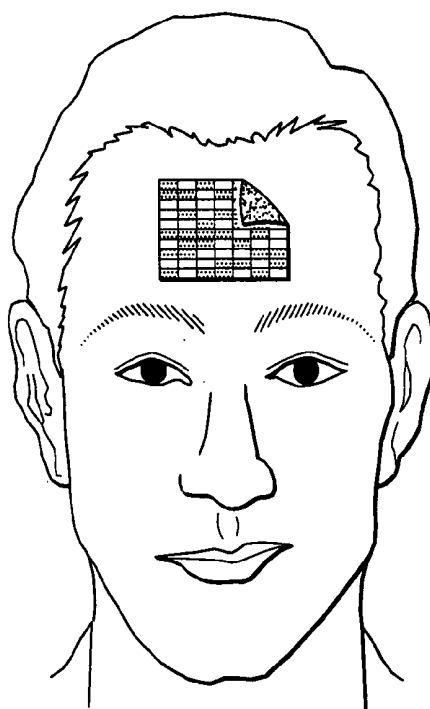
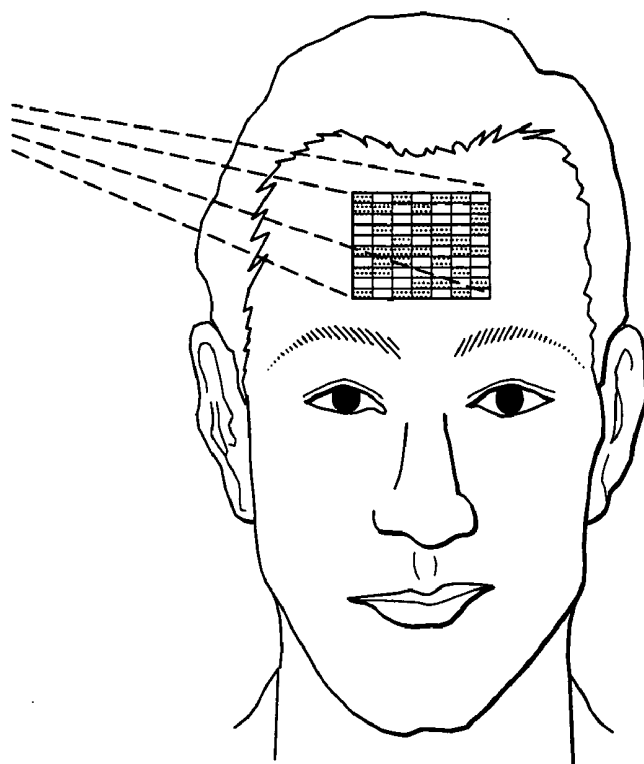
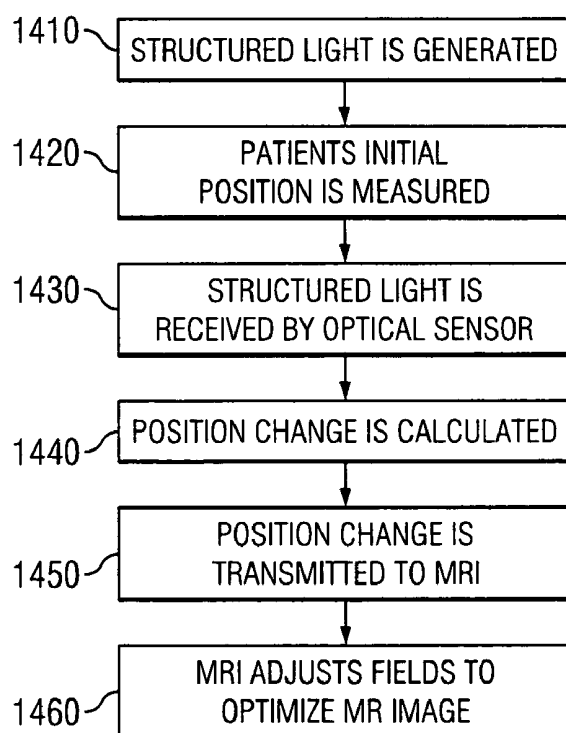
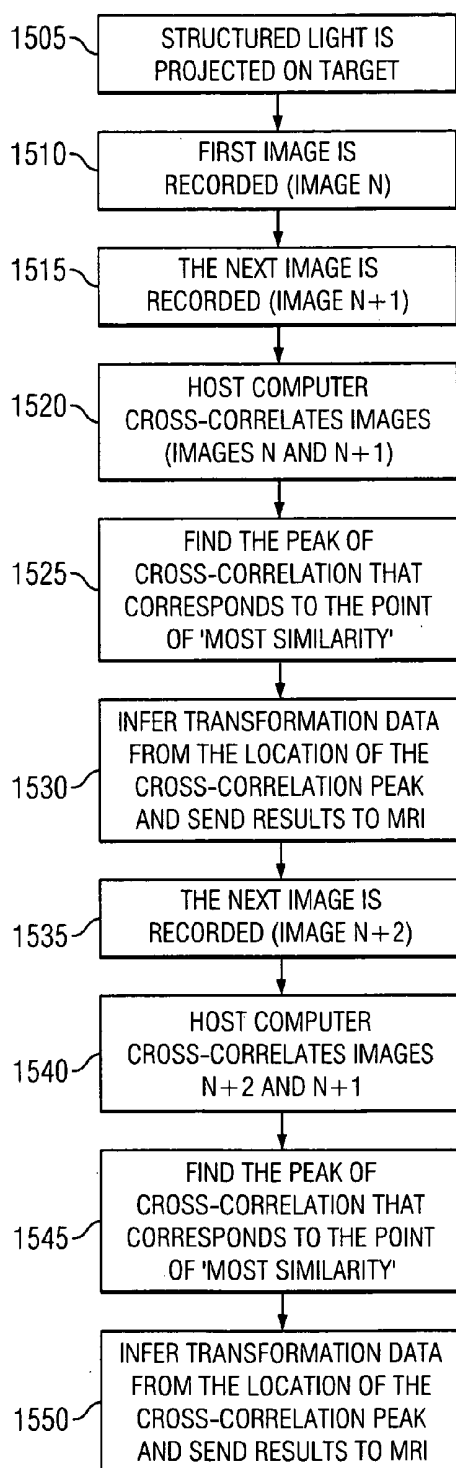
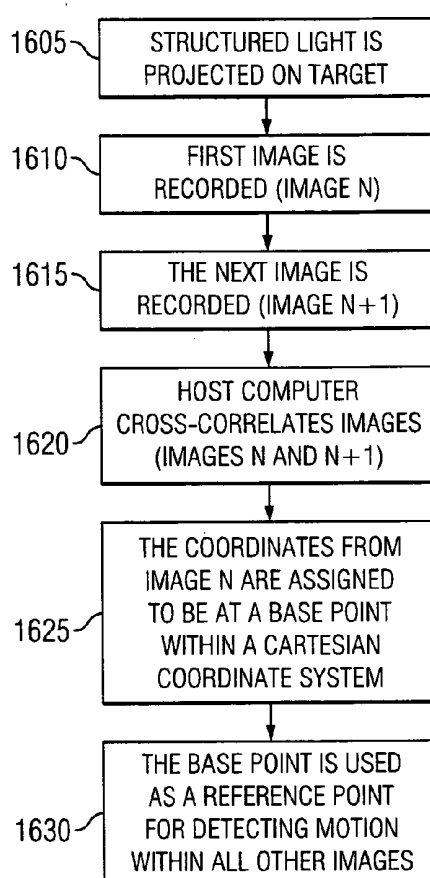


FIG. 12

*FIG. 13**FIG. 14*

*FIG. 15**FIG. 16*

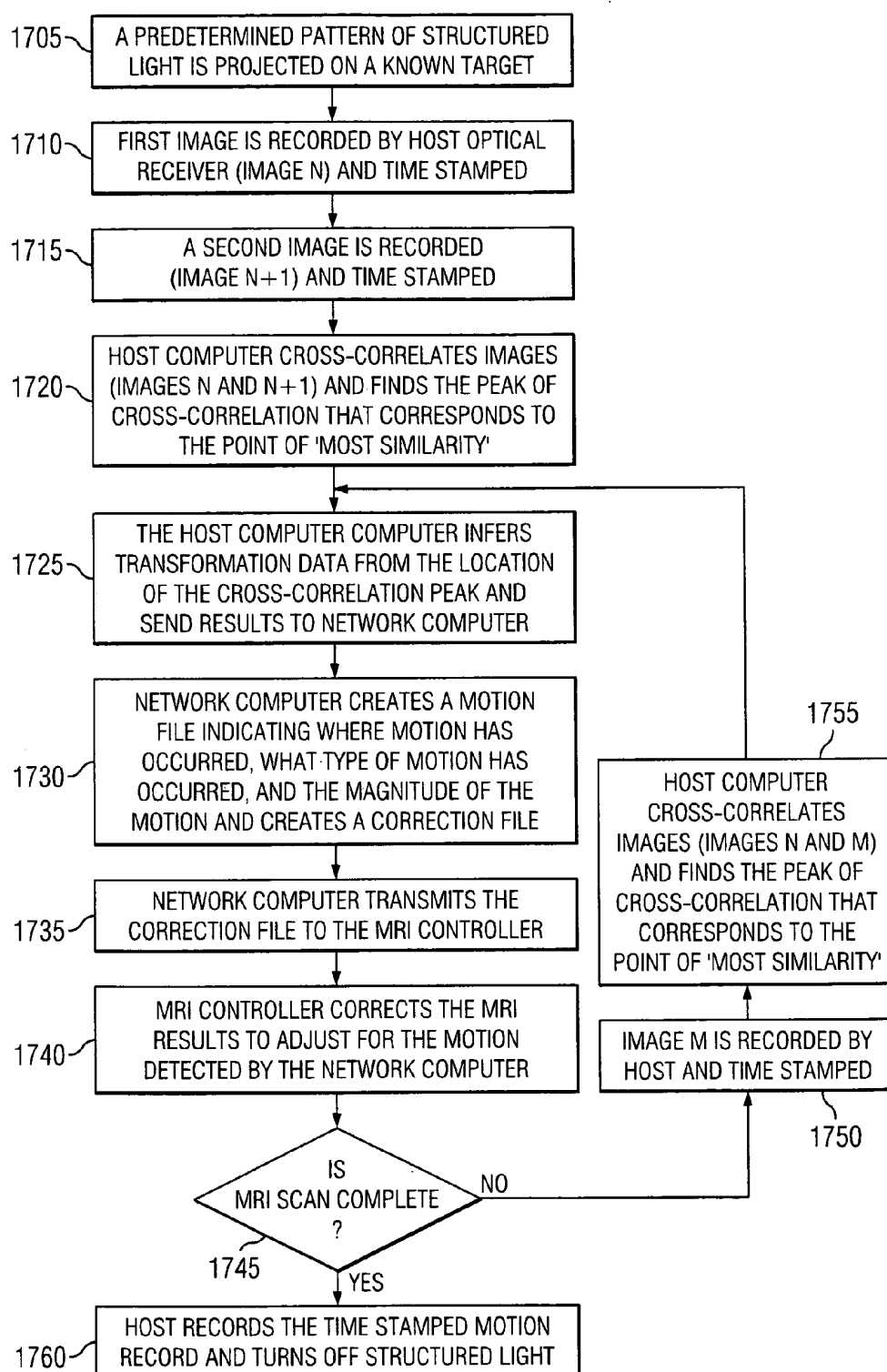
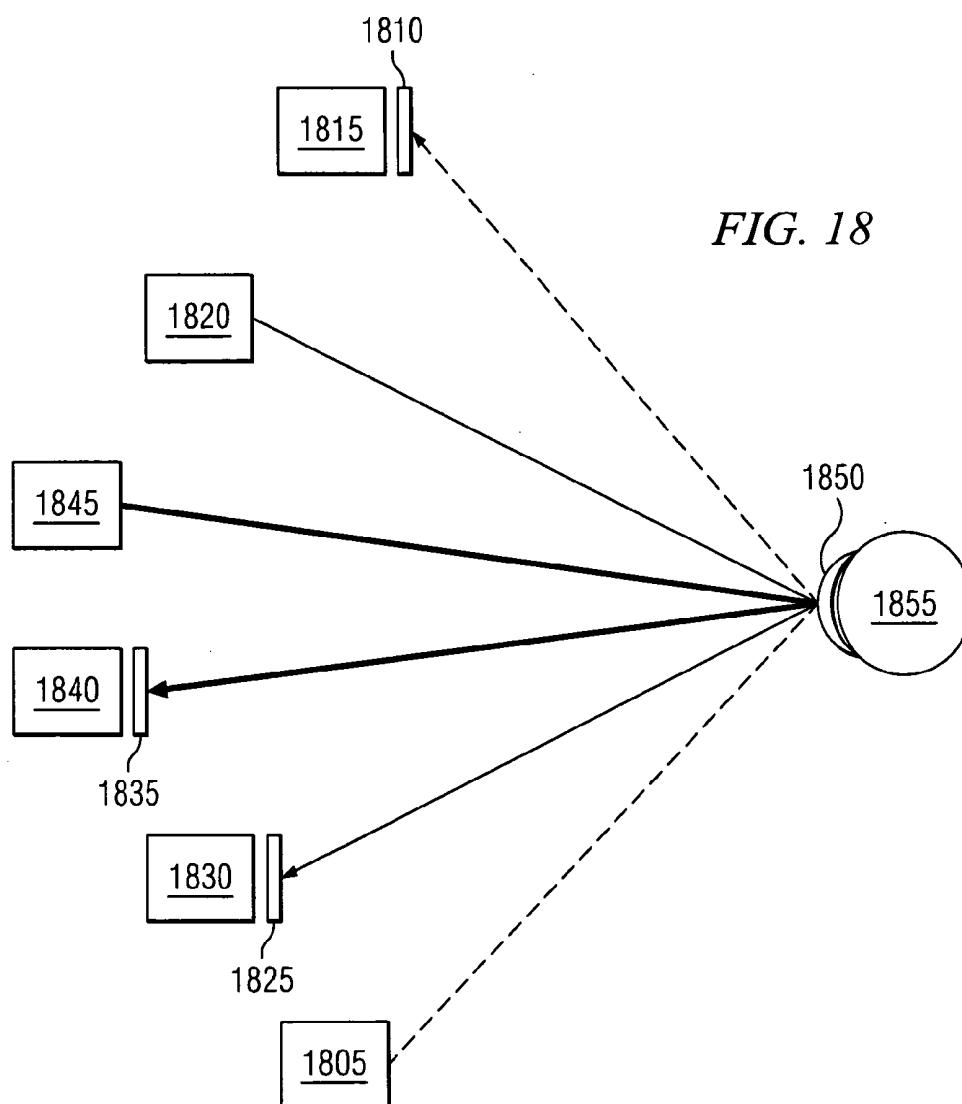


FIG. 17



METHOD FOR DETERMINING LOCATION AND MOVEMENT OF A MOVING OBJECT

CROSS REFERENCE TO RELATED APPLICATIONS

[0001] This application is a Continuation-In-Part claiming priority benefit from U.S. patent application Ser. No. 11/282, 046 which was filed on Nov. 16, 2005.

TECHNICAL FIELD OF THE INVENTION

[0002] The present invention relates, in general, to the field of motion tracking, and in particular to head tracking in a magnetic resonance imaging application. In particular the invention teaches an apparatus and method to track the movement of a target in three-dimensional space during medical imaging scanning using optical technology. The invention further comprises an apparatus and method to use the head tracking data to control the magnetic field gradients and/or radio frequency fields of the magnetic resonance imaging instrument thereby maintaining active image registration during the scans.

BACKGROUND OF THE INVENTION

[0003] Computerized tomography (CT), magnetic resonance imaging (MRI), and positron emission tomography (PET), coupled with developments in computer-based image processing and modeling capabilities have led to significant improvements in the ability to visualize anatomical structures in human patients. This information has become invaluable in the diagnosis, treatment, and tracking of patients. The technology has been recently been expanded to be used in conjunction with real-time interventional procedures.

[0004] MRI is the method of creating images (referred to as MR images) of the internal organs in living organisms. The primary purpose is demonstrating pathological or other physiological alterations of living tissues. MRI has also found many niche applications outside of the medical and biological fields such as rock permeability to hydrocarbons and certain non-destructive testing methods such as produce and timber quality characterization. Superb image contrast for soft tissues and millimeter scale spatial resolution has established MRI as a core imaging technology in most medical centers. MRI is unique among imaging modalities in that any one of a multitude of tissue properties can be extracted and highlighted.

[0005] The MRI process requires a highly accurate and stable target which to image. This is a consequence of the process by which medical MRI functions. Medical MRI most frequently relies on the relaxation properties of excited hydrogen nuclei in water. When the object to be imaged is placed in a powerful, uniform magnetic field, the spins of the atomic nuclei with non-zero spin numbers within the tissue all align in one of two opposite directions: parallel to the magnetic field or antiparallel.

[0006] The difference in the number of parallel and antiparallel nuclei is only about one in a million. However, due to the vast quantity of nuclei in a small volume, the nuclei sum to produce a detectable change in field strength. The magnetic dipole moment of the nuclei then moves in a gyrating fashion around the axial field. While the proportion is nearly equal, slightly more nuclei are oriented at the low energy angle. The frequency with which the dipole moments process is called the Larmor frequency. The tissue is then briefly exposed to

pulses of electromagnetic energy (RF pulse) in a plane perpendicular to the magnetic field, causing some of the magnetically aligned hydrogen nuclei to assume a temporary non-aligned high-energy state.

[0007] In order to selectively image the different voxels (3-D pixels) of the material in question, three orthogonal magnetic gradients are applied. The first is the slice selection, which is applied during the RF pulse. Next comes the phase encoding gradient, and finally the frequency encoding gradient, during which the tissue is imaged. Most of the time, the three gradients are applied in the X, Y, and Z directions of the machine. As a consequence of this methodology, any small shift in the position of the patient with respect to these fixed gradient axes will alter the orientations and positions of the selected slices.

[0008] In order to create an MR image, spatial information must be recorded along with the received tissue relaxation information. For this reason, magnetic fields with an intensity gradient are applied in addition to the strong alignment field to allow encoding of the position of the nuclei. A field with the gradient increasing in each of the three dimensional planes is applied in sequence. This information is then subsequently subjected to a Fourier transformation by a computer that transforms the data into the desired image and yields detailed anatomical information results.

[0009] With conventional anatomic MR imaging, the presence of moving biological tissue is problematic. The tissue produces image artifacts, degrades the quality of the images, and complicates the interpretation of MR images. The typical appearance of such image artifacts takes the form of "blurring," or a characteristic "motion ghost" in the phase encoding direction associated with incorrectly encoding the spatial frequencies of a moving object that is assumed to be static.

[0010] The typical medical resolution is about 1 mm, while research models can exceed 0.1 mm. Through the process of MRI, anatomy can be defined in great detail, and several other biophysical and metabolic properties of tissue, including blood flow, blood volume, elasticity, oxygenation, permeability, molecular self-diffusion, anisotropy, and water exchange through cell membranes, can also be represented. Conventional anatomical MR imaging uses this spin-echo, gradient-echo, and inversion recovery sequencing. There are other methods of MR that are currently being used, including magnetic resonance spectroscopy (MRS), apparent diffusion coefficient (ADC) mapping, diffusion-weighted imaging (DWI) and its derivatives of diffusion tensor imaging and tractography, perfusion imaging, permeability imaging, MR angiography (MRA), and functional MRI (fMRI). As the techniques of MR become more precise, there is corresponding need for increased accuracy and the tracking of the patient during the MR procedure. See E. Fukushima and S. B. W. Roeder, *Experimental Pulse NMR* Addison-Wesley, Reading, MA 1981; T. C. Farrar, *An Introduction To Pulse NMR Spectroscopy* Farragut Press, Chicago, 1987; R. C. Jennison, *Fourier Transforms and Convolutions* Pergamon Press, NY 1961; E. O. Brigham, *The Fast Fourier Transform* Prentice-Hall, Englewood Cliffs, NJ 1974; and A. Carrington A. D. McLachlan, *Introduction To Magnetic Resonance* Chapman and Hall, London 1967 which are each hereby incorporated by reference.

[0011] Functional MRI (fMRI) measures signal changes in the brain that are due to changing neural activity. This scan is completed at a low resolution but at a very rapid rate (typically once every 1-3 seconds). Increases in neural activity

cause changes in the MR signal via a mechanism called the BOLD (blood oxygen level-dependent) effect. Increased neural activity causes a corresponding increased demand for oxygen, which is responded to by the vascular system, which increases the amount of oxygenated relative to deoxygenated hemoglobin. Because deoxygenated hemoglobin attenuates the MR signal, the vascular response leads to a signal increase that is related to the neural activity. The use of MRI to measure physiologic and metabolic properties of tissue non-invasively requires dynamic imaging to obtain time-series data.

[0012] One example of the use of fMRI is to measure brain activity. This use relies on a well-established neurovascular coupling phenomenon that results in transient increases in blood flow, oxygenation, and volume in the vicinity of neurons that are functionally activated above their baseline level. Signal changes due to the blood oxygenation-level-dependent (BOLD) effect are intrinsically weak (only several percent signal change from baseline at 4.0 T or less). In addition, as BOLD imaging is typically coupled with a repetitive behavioral task (e.g., passive sensory, cognitive, or sensorimotor task) to localize BOLD signals in the vicinity of neurons of interest, there is significant potential for fMRI to be confounded by the presence of small head motions. Specifically, such motion can introduce a signal intensity fluctuation in time due to intra-voxel movement of an interface between two different tissues with different MR signal intensities, or an interface between tissue and air. Random head motion decreases the statistical power with which brain activity can be inferred, whereas task-correlated motion cannot be easily separated from the fMRI signal due to neuronal activity, resulting in spurious and inaccurate images of brain activation. In addition, head motion can cause mis-registration between neuroanatomical MR and fMR images that are acquired in the same examination session. This latter point is important because the neuroanatomical MRI data serve as an underlay for fMRI color maps, and mis-registration results in mis-location of brain activity. An analogous problem exists for aligning anatomical and functional MR images performed on different days.

[0013] Lack of motion in current MRI examinations anatomic motion is not merely preferred, but is instead absolutely essential. Most aspects of human motor system performance require the patient to execute a movement as part of the behavioral task that is imaged to visualize brain activity. Movements can be very simple (e.g., self-paced finger tapping) or more complex (e.g., visually-guided reaching). Such examinations require both that the desired movement is performed in a well-controlled or well-quantified fashion, and also that the movement does not induce task-correlated head motion that confounds the ability to observe brain activity using fMRI. Perhaps the most complicated scenario involves combining use of virtual reality (VR) technology with fMRI, to determine brain activity associated with VR tasks for assessment and rehabilitation of impaired brain function. Such applications are important from the standpoint of "ecological validity" as they provide the opportunity to visualize brain activity associated with tasks that generalize well to everyday behavior in the real 3D-world. For example, position tracking would be required to provide realistic visual representation of a virtual hand operated by a data glove in a virtual environment.

[0014] The problem of motion tracking within an fMRI environment has been well documented in published medical literature describing various aspects of motion detection and

quantitation. See Seto et al., *NeuroImage* 2001, 14:284-297; Hajnal et al., *Magn Res Med* 1994, 31: 283-291; Friston et al., *Magn Res Med* 1996, 35:346-355; Bullmore et al., *Human Brain Mapping* 1999, 7: 38-48; Bandettini et al., *Magn Res Med* 1993, 30:161-173; Cox et al., *Comp Med Res* 1996, 29:162-173; Cox et al., *Magn Res Med* 1999, 42:1014-1018; Grootenboer et al., *NeuroImage* 2000, 11:49-57; Freire et al., *IEEE Trans Med Im* 2002, 21(5):470-484; Babak et al., *Magn Res Im* 2001, 19:959-963; Voklye et al. 1999, *Magn Res Med* 41:964-972, which are each incorporated by reference.

[0015] As the clinical applications of MRI expand, there is a concurrent requirement for improved technology to visualize and determine the position and orientation of moving objects in the imaging field. Improvements in position tracking technology are required to advance the resolution and quality of the MRI, including the ability to image the anatomy of a patient, the imaging of tissue functions, the use of MRI data for other imaging modalities, and interventional applications.

[0016] For anatomical and functional MRI applications, as well as interventional MRI, there is the additional need to register data from other imaging modalities to provide comprehensive and complementary anatomical and functional information about the tissue of interest. The registration is performed either to enable different images to be overlaid, or to ensure that images acquired in different spatial formats (e.g., MRI, conventional x-ray imaging, ultrasonic imaging) can be used to visualize anatomy or pathology in precisely the same spatial location. While some algorithms exist for performing such registrations, computational cost would be significantly reduced by developing technology that enables data from multiple different imaging modalities to be inherently registered by measuring the patient's orientation in each image with respect to a common coordinate system.

[0017] By detecting, tracking, and correcting for changes in movement, data acquisition can be synchronized to a specific target. As a consequence, MR data acquisition is gated to a specific position of the target, and by implication, to a specific position of a specific target region.

[0018] U.S. Pat. No. 6,067,465 to Foo, et al. discloses a method for detecting and tracking the position of a reference structure in the body using a linear phase shift to minimize motion artifacts in magnetic resonance imaging. In one application, the system and method are used to determine the relative position of the diaphragm in the body in order to synchronize data acquisition to the same relative position with respect to the abdominal and thoracic organs to minimize respiratory motion artifacts. The time domain linear phase shift of the reference structure data is used to determine its spatial positional displacement as a function of the respiratory cycle. The signal from a two-dimensional rectangular or cylindrical column is first Fourier-transformed to the image domain, apodized or bandwidth-limited, converted to real, positive values by taking the magnitude of the profile, and then transformed back to the image domain. The relative displacement of a target edge in the image domain is determined from an auto-correlation of the resulting time domain information.

[0019] There is often a need in neuroimaging to look for changes in brain images over long periods of time, such as the waxing and waning of MS lesions, progressive atrophy in a patient with Alzheimer's disease, or the growth or remission of a brain tumor. In these cases, the ability to determine the position of anatomy as a function of time is extremely impor-

tant to detect and quantify subtle changes. High-spatial resolution is a basic requirement of 3D brain imaging data for patients with neurological disease, and motion artifacts a consequence of movement during scanning pose a significant problem. If a patient does not stay completely still during MR neuroimaging the quality of the MR scan will be compromised.

[0020] Many of the advantages of MRI that make it a powerful clinical imaging tool are also valuable during interventional procedures. The lack of ionizing radiation and the oblique and multi-planar imaging capabilities are particularly useful during invasive procedures. The absence of beam-hardening artifacts from bone allows complex approaches to anatomic regions that may be difficult or impossible with other imaging techniques such as conventional CT. Perhaps the greatest advantage of MRI is the superior soft-tissue signal contrast available, which allows early and sensitive detection of tissue changes during interventional procedures.

[0021] MR is used for procedures such as “interventional radiology”, where images produced by an MRI scanner guide surgeons in a minimally invasive procedure. However, the non-magnetic environment required by the scanner, and the strong magnetic radiofrequency and quasi-static fields generated by the scanner hardware require the use of specialized instruments. Exemplary of such endoscopic treatment devices are devices for endoscopic surgery, such as for laser surgery disclosed in U.S. Pat. No. 5,496,305 to Kittrell et al, and biopsy devices and drug delivery systems, such as disclosed in U.S. Pat. No. 4,900,303 and U.S. Pat. No. 4,578,061 to Lemelson.

[0022] Prior art attempts at tracking motion using cross-correlation and other simple distance measurement techniques have not been highly effective where signal intensities vary either within images, between images, or both. U.S. Pat. No. 6,292,683 to Gupta et al. discloses a method and apparatus to track motion of anatomy or medical instruments between MR images. The invention includes acquiring a time series of MR images of a region of interest, where the region of interest contains the anatomy or structure that is prone to movement, and the MR images contain signal intensity variations. The invention includes identifying a local reference region in the region of interest of a reference image and acquired from the time series. The local reference region of the reference image is compared to that of the other MR images and a translational displacement is determined between the local reference region of the reference image and of another MR image. The translational displacement has signal intensity invariance and can accurately track anatomy motion or the movement of a medical instrument during an invasive procedure. The translational displacement can be used to align the images for automatic registration, such as in myocardial perfusion imaging, MRA, fMRI, or in any other procedure in which motion tracking is advantageous. One of the problems with this invention, is that the application and implementation of this methodology has proven difficult.

[0023] Two implementations of this correction scheme have been disclosed. The first is where a correlation coefficient is calculated and used to determine the translational displacement, and one in which the images are converted to a binary image by thresholding (using signal intensity thresholds) and after computation of a filtered cross-correlation, a signal peak is located and plotted as the translational dis-

placement. Examples of techniques using this approach are shown in U.S. Pat. No. 5,947,900 (Derbyshire) and U.S. Pat. No. 6,559,641 (Thesen)

[0024] U.S. Pat. No. 6,516,213 to Nevo discloses a method and apparatus to determine the location and orientation of an object, while the body is being scanned by magnetic resonance imaging (MRI). Nevo estimates the location and orientation of various devices (e.g., catheters, surgery instruments, biopsy needles) by measuring voltages induced by time-variable magnetic fields in a set of miniature coils, said time-variable magnetic fields being generated by the gradient coils of an MRI scanner during its normal imaging operation. However, unlike the present invention, the system disclosed by Nevo is not capable of position tracking when imaging gradients are inactive, nor is it capable of measurements outside the sensitive volume of the imaging gradients.

[0025] A subset of all of the above correction schemes is currently conventionally employed in fMRI. As in anatomical MRI, these schemes remain an incomplete solution to the problem and the search for improved motion suppression continues. Typically, fast imaging is employed to “freeze” motion within the fMRI acquisition time frame, in combination with use of head restraints to limit motion. It is still possible to achieve poor activation image quality if patients exhibit task-correlated motion on the order of 1 millimeter. This problem is particularly manifest in specific patient populations (e.g. dementia, immediate post-acute phase of stroke). Furthermore, image-based coregistration algorithms suffer from methodological limitations. Consequently, the resulting co-registered images still can suffer from residual motion contamination that impairs the ability to interpret brain activity.

[0026] Another method of tracking the position of a patient in an MRI is disclosed in US Application 2005/0054910, published Mar. 10, 2005. In this approach, a reference tool is fixed to a stationary target as close as possible to the centre of the sensitive measuring volume of an MRI-compatible camera system. There are several drawbacks of this approach, including the requirement of a second “tracking” component that must be calibrated with a dummy object, the position ambiguity due to the configuration of this approach, and the inherent limitation of the resolution provided by this approach.

[0027] U.S. Pat. No. 6,879,160 to Jakab describes a system for combining electromagnetic position and orientation tracking with magnetic resonance scanner imaging. Jakab discloses a system where the location of a magnetic field sensor relative to a reference coordinate system of the magnetic resonance scanner is determined by a tracking device using a line segment model of a magnetic field source and the signal from a magnetic field sensor. However, resolutions provided by the Jakab invention are not as precise as is possible.

[0028] There is consequently a need for improved patient movement tracking techniques in medical imaging. There is a need for improved patient movement tracking that can function in adverse environments including high strength magnetic and/or radio frequency fields without the tracking mechanism exerting its own RF pulse or magnetic field. There is a need for improved patient movement tracking techniques that can be performed in real time. In particular, but without limitation, there is a need for real time tracking of

a patient's head position in a high field strength fMRI without disrupting the scanning by the fMRI.

SUMMARY OF THE INVENTION

[0029] The present invention includes improvements to the field of tracking patient movement in an MRI application. An apparatus and method are taught to track the movement of a patient's head during medical imaging scanning using optical technology. Feedback control of the gradient and/or radiofrequency magnetic fields can provide real time correction of imaging data.

[0030] The following terms should be given the following meanings:

[0031] "Cross-correlation"—Cross-correlation is meant to include the process used to calculate the geometric translation differences between two separate and independent images. This process also compares two sequences of images on element-by-element bases and can provide the point of peak of most similarity.

[0032] "Structured light"—Structured light is meant to include patterns of light that are suitable for cross-correlation. Generally speaking this may include a bundle of light rays that may be patterned or structured in order to enhance the performance of an optical measurement. Typically, the encoding of structured light is predetermined, so that the record of optical data can be optimally processed for spatial measurements. Examples of structured light may include, but are not limited to, amplitude encoding, phase encoding, or a chromatic (or color) encoding.

[0033] "Phase correlation"—Phase correlation is meant to include the method of taking the Fourier Transform of two or more images and correlating the relative phases to find rotation or scale between them.

[0034] "Laser"—The term laser includes illumination sources of sufficient intensity to drive detector optics to get a result. The illumination sources can include broadband sources such as incandescent lamps and flashbulbs. Narrow-band sources are also included such as gas discharge lasers or solid-state compound ataxia lasers. Illumination sources can also include LEDs and/or arrays of LEDs. Illumination sources can further include sources of selected wavelength ranges or groups of ranges.

[0035] One embodiment of the instant invention is a system that is taught used in conjunction within an MRI machine that uses a predetermined pattern placed or projected onto a patient's head to track movement of a patient during an MRI scan. Optical systems incorporating structured light and a processor record the position and movement of the pattern and are able to perform mathematical analysis of the pattern to determine the positional shift of the patient. Weighted averages, Fourier transforms, Hadamard matrices and cross-correlation of data related to X-Y translation, rotation and scaling of the image of the pattern are used to analyze movement of the patient's head. Feedback related to the movement is provided to the MRI machine that allows for adjustments in focusing coils for real time tracking of the patient's movements during the MRI procedure. As a result, the MRI procedure becomes more accurate as it is adjusted for the patient's movements.

BRIEF DESCRIPTION OF THE DRAWINGS

[0036] For a more complete understanding of the features and advantages of the present invention, reference is now

made to the detailed description of the invention along with the accompanying figures in which corresponding numerals in the different figures refer to corresponding parts and in which:

[0037] FIG. 1 is example of pseudo Matlab code that can be used in the weighted average approach of comparing two images.

[0038] FIG. 2 is example of pseudo Matlab code that can be used in the cross correlation of two images.

[0039] FIG. 3 is illustration of the conversion between different coordinate systems.

[0040] FIG. 4 is example of pseudo Matlab code that can be used in the Fourier-Mellin approach of comparing two images.

[0041] FIG. 5 is a schematic illustration of a head tracking apparatus comprising a light source, structured light generated between the light source and the conveying light path, an object to be imaged, and a detector array.

[0042] FIG. 6 is a schematic illustration of a head tracking apparatus comprising a light source, structured light generated in the conveying light path, an object to be imaged, and a detector array.

[0043] FIG. 7 is a schematic illustration of a head tracking apparatus comprising a light source, structured light that is generated between the conveying light path and the object to be tracked, the object to be imaged, and a detector array.

[0044] FIG. 8 is a schematic illustration of a head tracking apparatus comprising a light source, a structured light generator at the object to be imaged, the object to be imaged, and a detector array.

[0045] FIG. 9 is a block diagram of a head tracking apparatus used to provide active feedback to the measurement fields of the MRI.

[0046] FIG. 10 is a flow chart illustrating a method of head tracking.

[0047] FIG. 11 is an illustration of one predetermined target that can be used to with structured light.

[0048] FIG. 12 is an illustration of a predetermined target being placed onto a patient's forehead.

[0049] FIG. 13 is an illustration of a predetermined target being projected onto a patient's forehead.

[0050] FIG. 14 is a flow chart illustrating a method of providing active feedback to the measurement fields of the MRI based on head tracking data.

[0051] FIG. 15 is a flow chart illustrating a translation detection algorithm.

[0052] FIG. 16 is a flow chart illustrating a calibration algorithm.

[0053] FIG. 17 is a flow chart illustrating one preferred embodiment of image correlation.

[0054] FIG. 18 is an illustration of a target comprised of three patterns made up of different dyes irradiated by sources of different frequencies.

DETAILED DESCRIPTION OF THE INVENTION

[0055] While the making and using of various embodiments of the present invention are discussed in detail below, it should be appreciated that the present invention provides many applicable inventive concepts which can be embodied in a wide variety of specific contexts. The specific embodiments described herein are merely illustrative of specific ways to make and use the invention and do not delimit the scope of the invention.

[0056] In one embodiment of the instant invention is a system that is used in conjunction within an MRI machine that uses a predetermined pattern placed or projected onto a patient's head to track movement of a patient during an MRI scan. Optical systems record the position and movement of the pattern and are able to perform mathematical analysis of the pattern to determine the positional shift of the patient.

[0057] In this preferred embodiment, light is projected onto a target that reflects some of the light into an optical receiver. One of the innovations of the present inventions is the use of structured light. Structured light consists of an orderly pattern of rays of light that is suitable for cross-correlation. Examples of methods to create structured light include, but are not limited to, using of a laser to create a speckle pattern, a spatial filter using a projector to convey the structured light pattern (an example would be with use of a patterned slide), and using a light source directed towards an area with a known pattern. Other examples are an array of light emitters either positioned as a projector towards the target or as a light emitting tag placed on the target. Another example is a spatial light modulator used in the path of projected light such as a liquid crystal display or a MEMS device. Chemically patterned light emitting tags can also be used. Examples of these devices are a light emitting tag containing patterns created by phosphorescent paint, inks or dyes. Other examples include various fluorophores used in inks or dyes such as phthalocyanine and naphthacyanine. In embodiments where inks and dyes are used with frequency shifting capabilities such as up converters and down converters, illuminating light should match the frequencies at which the tag produces light in detectable levels.

[0058] Since motion detection was implemented using a cross-correlation algorithm, any form of similarity within the structured light would adversely influence the robustness of the algorithm. Therefore, any regularity or order in the pattern would produce multiple peaks in the cross-correlation thus making it difficult to decide upon the highest one. This embodiment avoids the problem of similarity within the projected light source by the use of an optimized pattern of structured light.

[0059] Many algorithms and methods of signal processing can be employed by the present invention in order to determine and track movement of the structured light received either from the target or from the structured light generator. The preferred embodiment uses weighted averages, cross-correlation, Fourier-Mellin, phase correlation and image maximization to determine movement. Of course, other signal processing methods known in the art will suffice. A weighted average is one method used to calculate X and Y translational motions. The method treats every black pixel as a one and every light pixel as a zero. A pixel is considered black if its RGB value exceeds a certain preset value. In addition, a pixel is considered white if its RGB value is lower than a certain preset value. The algorithm calculates the center of the image's imaginary weight in much the same way as a center of mass would be calculated. The algorithm calculates the weighted average of the columns and rows. When the pattern translates in two-dimensional space, the weighted average stays at the same place within the pattern. This allows for the determination of the amount of translation that has occurred between the two images. One example of an implementation of this weighted average approach in a software application such as Matlab is given in FIG. 1.

[0060] Standard cross-correlation is another method that can be used to calculate the X and Y translation differences of

the images. Cross-correlation compares two sequences of images of a single target on an element-by-element basis and is able to provide the point or peak of "most similarity". By calculating the coordinates of this peak, it is possible to find the translation between the two images. Cross-correlation of two images can be imagined as sliding one three dimensional image over another until a perfect fit is found. The cross-correlation of two complex functions $f(t)$ and $g(t)$ of a real variable t , denoted fHg is defined by the following equation where $*$ denotes convolution and \bar{f} is the complex conjugate of $f(t)$:

$$f^*g = \bar{f}(-t) * g(t),$$

[0061] One example of an implementation of this cross-correlation approach in a software application such as Matlab is given in FIG. 2.

[0062] In another embodiment, the cross-correlation of rotation is found by using a Fourier-Mellin algorithm. Fourier-Mellin method transforms Cartesian coordinates to polar coordinates and correlates the Fourier Transform of the two images to find the angle of rotation. One illustration of the difference in the coordinate systems is given by FIG. 3. The traditional definition of the Fourier-Mellin transform is:

$$f(t) = \frac{1}{2\pi i} \int_{c-i\infty}^{c+i\infty} F(s) e^{st} ds, t > 0,$$

[0063] The Fourier-Mellin transform is invariable in translation, rotation, and scale. The Fourier-Mellin method consists of four steps. First, the FFT (Fast Fourier Transform) of an image is taken. A FFT is a discrete Fourier transform algorithm which reduces the number of computations needed for N points from (N^2) to $(2 * N * (\lg N))$, where \lg is the base-2 logarithm. If the function to be transformed is not harmonically related to the sampling frequency, the response of an FFT looks like a sinc function (although the integrated power is still correct). Aliasing (leakage) can be reduced by apodization using a tapering function. However, aliasing reduction is at the expense of broadening the spectral response.

[0064] The second step of the Fourier-Mellin transform is involves the step of taking the Cartesian coordinates and converting them to Log-Polar coordinates. This allows for a correlation between translation in the Fourier-Mellin domain and rotation in Cartesian domain.

[0065] Third, the Mellin Transform is taken. The Mellin transform is an integral transform that and is generally regarded as the multiplicative version of the two-sided Laplace transform. The general equation for a Mellin transform on an equation $f(t)$ is:

$$\{Mf\}(s) = \varphi(s) = \int_0^\infty x^s f(x) \frac{dx}{x}.$$

[0066] Finally, the data from the output is analyzed to determine the point of most similarity and adjustments for movement may be made. One example of an implementation of this Fourier-Mellin approach in a software application such as Matlab is given in FIG. 4.

[0067] Another signal processing method used is Phase Correlation. Phase Correlation consists of taking the Fourier Transform of the two images and correlating the relative

phases to find rotation or scale. Phase correlation is another technique that utilizes a Fast Fourier Transform or FFT.

[0068] By taking the two dimensional FFT of an image, phase information can be visualized. One equation used to acquire the FFT of an image is:

$$f_j = \sum_{k=0}^{n-1} e^{-2\pi i j(k/n)} x_k$$

[0069] In two dimensions, the x_k can be viewed as an $n_1 \times n_2$ matrix. The algorithm corresponds to first performing the FFT of all the rows and then of all the columns (or vice versa).

[0070] In the phase correlation technique, it is possible to compare the phases of the two images to detect the difference between the two images. By determining the point where the phases are at the maximum congruency, it is possible to determine the angle of rotation between two images. By analysis of the transform, the phase information that is contained in an image is acquired. The change in the phase information holds the key to determining the rotation angle of the image. The peak in the middle of the graph corresponds to the point of most congruency of the phases of the two images, and gives the change in angle that the image has undergone. The phase correlation algorithm was utilized using the following steps. First, the discrete FFT of two images is calculated. Second, the conjugate of the second image is taken. Third, the Fourier transforms are multiplied together element-wise. Fourth, the product of this multiplication is normalized element-wise. Fifth, the normalized cross power spectrum inverse transform is performed. Sixth, the peak of the inverse transform is taken. This step may include using sub-pixel methods to determine where a peak is found.

[0071] In one preferred embodiment, the results from the structured light were optimized by maximizing the percentage of the image taken up by structured light without the structured light exceeding the boundaries of the target image. This preferred upper boundary (i.e. the structured light staying within the target image) is a result of the reliance by the cross-correlation algorithms on a pixel-by-pixel comparison of two images. Since the algorithm compares structured light, it is desirable to achieve the best ratio of pixels per structured light element. If the structured light takes up 100% of the image, no change can be perceived between the structured light and the surrounding environment. If the size of the structured light is too big (90%), different translational and rotational motions might take some of the structured light out of the field of view of the camera thus contributing to loss of information contained in the structured light. On the other hand, if the structured light constitutes too little (1%) of the overall image, cross-correlation and Fourier-Mellin algorithms will not be robust enough to perform precise calculations.

[0072] In FIG. 5, one preferred embodiment is shown. Light is generated with coherent laser 520. The light passes through structured light generator 530 that is located between light source 520 and conveying light path 540. Structured light generator 530 could be implemented as, but not limited to, a speckle pattern, a spatial filter, a slide, an array of light emitters, or a spatial light modulator based, for example, on a liquid crystal or a MEMS device. The structured light travels through conveying path 540 to object to be imaged 550. Conveying path 540 could be an image preserving optical

fiber, free space, or any medium which does not disrupt the transmission of the structured light. The structured light appears on object to be imaged 550. Next the structured light is reflected onto return light path 560 which could be an image preserving optical fiber, free space, or any medium which does not disrupt the transmission of the structured light. If return light path 560 is free space, image optics have to be correctly determined using lenses, mirrors or other optical train as would be well known in the art. The light arrives at analyzer 570, which could be a filter or polarizer before entering detector array 580. In this embodiment, detector array 580 is implemented as a CCD camera. One exemplary part that could be used is a Digital Rebel XT made by Canon. The structured light pattern is used to detect the movement of object 550.

[0073] FIG. 6 shows another preferred embodiment. Light is generated with coherent laser 620. It enters conveying light path 640. Conveying light path 640 could be a multimode fiber or any medium that does not disrupt the transmission of the structured light. Inside conveying light path 640, a structured light pattern is generated, for example a speckle pattern. The structured light appears on object to be imaged 650. Next the structured light goes into return light path 660, which could be an image preserving fiber, example-coherent bundle, free space, or through any medium which does not disrupt the transmission of the structured light. If return light path 660 is free space, image optics have to be correctly determined using lenses, mirrors or other optical train as would be well known in the art. The structured light enters detector array 670 which, in this embodiment, is implemented as a CCD camera. The structured light pattern is used to detect the movement of the object 650.

[0074] In FIG. 7, another preferred embodiment is shown. Light is generated with coherent laser 720. The light travels on conveying path 740 to structured light generator 730 that is located between conveying light path 740 and object to be imaged 750. Conveying light path 740 could be an optical fiber, free space, or any medium that does not disrupt the transmission of the structured light. Structured light generator 730 could be implemented as, but not limited to, a speckle pattern, a spatial filter, a slide, an array of light emitters, or a spatial light modulator based, for example, on a liquid crystal or a MEMS device. The structured light appears on object to be imaged 750. Next the structured light goes into return light path 760 which could be an image preserving fiber, example-coherent bundle, free space, or any medium that does not disrupt the transmission of the structured light. If return light path 760 is free space, image optics have to be correctly determined using lenses, mirrors or other optical train as would be well known in the art. The light arrives at analyzer 770, which could be a filter or polarizer before entering detector array 780. Detector array 780 is implemented in this embodiment as a CCD camera. The structured light pattern is used to detect the movement of object 750.

[0075] In FIG. 8, another preferred embodiment is shown. Light is generated with coherent laser 820. The light travels on conveying path 840 to structured light generator 850 that is located on the object. Structured light generator 850 is a reflective material that produces structured light; an example would be a tag with a high-resolution matrix on it, or a hologram. The structured light appears on object to be imaged 860. Next the structured light goes into return light path 870. If return light path 870 is free space, image optics have to be correctly determined using lenses, mirrors or other optical

train as would be well known in the art. The light arrives at analyzer **880**, which could be a filter or polarizer before entering detector array **890**. The filter can be responsible for selectively allowing a specified frequency of light to reach the detector. In this embodiment, detector array **890** is implemented as a CCD camera. The structured light pattern is used to detect the movement of object **860**.

[0076] In yet another preferred embodiment, structured light generator **850** is a physical target with the ability to independently produce a structured light pattern. In this embodiment, a matrix of high intensity LED devices is arranged in the pattern to transmit a structured light beam to a receiver.

[0077] In another embodiment, structured light generator **850** is a tag which has impressed on it a laser luminophore such as a polycyclic chemical compound that is usually characterized as fluorescent. Fluorophores are also suitable. Suitable laser luminophores are available as laser pumped dyes sold for example by Lambda Physik Goettingen, Germany. Typical laser luminophores display fluorescence in the range of 300 to 2500 nm and have a peak width of about 200 nm. Suitable dyes are applied to a reflective tag in a pattern which produces structured light when illuminated with radiation and wavelengths which produced fluorescence. Light sources such as laser light sources emitting in the 200 to 600 nm range are suitable. The most preferred sources include XeCl-excimer lasers (309 nm), nitrogen lasers (337 nm) and Nd:YAG (335 nm). Other preferred light sources LEDs which generally emit light in a wavelength range of about 400 to 600 nm. Chemical compounds useful as fluorophores in this embodiment include polycyclic hydrocarbons including catacondensed and pericondensed aromatics, heterocyclic hydrocarbons, including condensed and substituted indoles, oxazoles, oxadiazoles and furan compounds and xanthone and xanthone derivatives including condensed systems, acids and salts. Representative laser luminophores which are useful in this embodiment include p-quaterphenyl, perchlorate benzoic acid, monohydrochloride. Of course, other laser luminophores and fluorophores will also suffice. Representative laser luminophores which are useful in this embodiment include p-quaterphenyl, perchlorate benzoic acid, monohydrochloride. Of course, other laser luminophores will also suffice.

[0078] In yet another embodiment, visible dyes and invisible dyes such as laser luminophores or fluorophores are used on a tag in different or similar patterns. Illuminating radiation of different frequencies can then be used to produce reflectances in structured light of different frequencies so that changes in motion of the structured light generator can be detected in two frequencies at the same time. The redundancies are available allow more accurate determination of movement of the structured light generator.

[0079] In FIG. 18, another preferred embodiment is shown. Structured light generator **1850** in this embodiment is a physical tag having three different patterns impressed on it with dyes including a visible dye, a laser luminophore dye, and a fluorophore. Each of the patterns is different. Light is generated corresponding to the first dye by light source **1805**. Reflected light from light source **1805** impinges on structured light generator **1850** and is reflected toward filter **1810** and receiver **1815**. Filter **1810** is designed to tune the light received from structured light generator **1850** to a frequency receptive to the laser luminophore dye. Light source **1820** produces light at a certain different frequency which

impinges on structured light generator **1850** and is reflected toward filter **1825** and receiver **1830**. Filter **1825** is designed to tune the light from light source **1820** to the frequency of the fluorophore included in structured light generator **1850**.

[0080] Light source **1830** generates light at a third frequency which impinges on structured light generator **1850** and is reflected at a certain visible frequency toward filter **1835** and receiver **1840**. Filter **1835** is designed to tune the reflected light from tag **1850** to a visible frequency. Each of the receivers is capable of registering the pattern produced by a specific dye on structured light generator **1850**.

[0081] In a block diagram of head tracking apparatus **910** providing active real time feedback to the measurement fields of MRI instrument **980** is shown. Light is generated with head tracking apparatus **910**. The structured light travels on conveying path **920** to object **930** under analysis. Next the structured light goes into return light path **940** which could be an image preserving fiber, example-coherent bundle, or free space. The structured light is registered at head tracking apparatus **910** and sent to interface **960** between MRI instrument **980** and the head tracking apparatus via information-carrying channel **950**. Interface **960** can be implemented as a computer. Interface **960** calculates the change in position of object **930** under analysis and sends the information to MRI instrument **980** via information carrying channel **970**. MRI instrument **980** adjusts the fields according to the new position information. This is accomplished in real time between successive scans of the MRI instrument.

[0082] In FIG. 10, a flow chart illustrating the method of head tracking is shown. In the first phase structured light is generated **1010**. In the second phase, structured light is used to measure position **1020** of the object. In the third phase, the object moves and the received structured light **1030** pattern changes. In the fourth phase, the change in the received structured light pattern is calculated **1040**.

[0083] The object for the structured light to be focused on may be created in a number of ways depending on the embodiment chosen. One preferred embodiment is the use of a random monochromatic pattern that is used as a target. FIG. 11 is an example of one target that may be used to optimize the results from structured light. FIG. 12 is an illustration of the technique of placing this type of target pattern or tag onto a patient's forehead. FIG. 13 is an illustration of the technique of projecting this type of pattern onto a patient's forehead. One exemplary part that can be used for projection is an EP 751 DLP made by Optima.

[0084] In FIG. 14, a flow chart illustrating the method of providing active feedback to the measurement fields of the MRI based on the head tracking data is shown. In the first phase structured light is generated **1410**. In the second phase, structured light is used to measure position **1420** of the object. In the third phase, the object moves and the received structured light **1430** pattern changes. In the fourth phase, the change in the received structured light pattern is calculated **1440**. In the fifth phase, the calculated change in the position of the object is sent to MRI instrument interface **1450**. In the sixth phase, interface **1450** communicates with the MRI instrument to adjust the fields of the MRI to improve scan **1460**. This is accomplished in real time between successive scans of the MRI instrument.

[0085] FIG. 15 is a flow chart illustrating one implementation of the Translation Detection Algorithm. Structured light is projected on target **1505**. A first image is recorded (image N) **1510**. Another image is then recorded (image N+1) **1515**.

Host computer cross-correlates images (images N and N+1) **1520**. The host computer finds the peak of cross-correlation that corresponds to the point of 'most similarity' **1525**. The host computer infers transformation data from the location of the cross-correlation peak and sends results to the MRI **1530**. The next image is recorded (image N+2) **1535**. Host computer cross-correlates images N+2 and N+1 **1540**. Find the peak of cross-correlation that corresponds to the point of 'most similarity' **1545**. Infer transformation data from the location of the cross-correlation peak and send results to MRI **1550**.

[0086] FIG. 16 is a flowchart illustrating a possible method of calibration. Structured light is projected on target **1605**. The first step is for a first image is recorded **1610**. The next step is for a second image is recorded (image N+1) **1615**. The host computer cross-correlates acquired images **1620**. The coordinates from image N are assigned to be at a point based in Cartesian coordinate system **1625**. This point can be used as a reference point for all further image calculation.

[0087] FIG. 17 is a flowchart illustrating another method of using structured light to correct for motion data. In this embodiment, there are three separate components: a host connected to an optical receiver capable of receiving, processing, and cross-correlating images, a network computer to create a motion file based on information obtained from the host computer, and an MRI controller capable of interfacing with the network computer to accept data from the network computer and correct MRI results based upon data obtained by the network controller.

[0088] In the embodiment that is illustrated by FIG. 17, the first step is to project a predetermined pattern of structured light onto target, where the area of the structured light is less than the area of the pattern, and where the structured light falls completely within the target **1705**. Structured light is reflected off the target and into the host optical receiver, and an image (image N) is captured by host optical receiver and time stamped **1710**. The next step is for a second image to be recorded (image N+N) and time stamped **1715**. The host computer cross-correlates images (images N and N+1) and finds the peak of cross-correlation that corresponds to the point of 'most similarity' **1720**. The host computer infers transformation data from the location of the cross-correlation peak and sends results to network computer **1725**. The network computer creates a motion file indicating where motion has occurred, what type of motion has occurred, and the magnitude of the motion and creates correction file **1730**. The network computer transmits the correction file to MRI controller **1735**. The MRI controller corrects the MRI results to adjust for the motion detected by the host computer by using the time stamps on each image taken by the MRI to the motion data time stamped by host computer **1740**. If the MRI scan is complete, the host turns off structured light **1760**. If the MRI scan is not complete, image M is recorded by host and time stamped **1750**. The host computer cross-correlates images (images N and M) and finds the peak of cross-correlation that corresponds to the point of 'most similarity' **1755**. The host computer infers transformation data from the location of the cross-correlation peak from the original image N and the new image M and sends results to network computer **1725**.

[0089] It is envisioned that the embodiment illustrated by FIG. 17 could be modified to allow for the three components (e.g. network computer, host computer, and MRI controller) to be integrated into one or more components. It is further envisioned that one computer to accomplish one or more of

the tasks, i.e. a central computer both capture and process images and transmit the data directly to an MRI. It is further envisioned by the inventors that the comparison in images could be made from the each previous image in the sequence rather than from the first image to give a clearer view of subtle changes in movement.

[0090] It is further envisioned that there are other methods to use structured light patterns; i.e. electronic detection patterns such as sensors attached to the patient's head that could be used as an alternative to optical receivers. Moreover, any number of different types of light source may be used to project light, including, but not limited to, strobe lights. It is further envisioned that in some embodiments target itself emanate light by the use of a target that emits light directly into an optical receiver.

[0091] While this invention has been described in reference to illustrative embodiments, this description is not intended to be construed in a limiting sense. Various modifications and combinations of the illustrative embodiments, as well as other embodiments of the invention, will be apparent to persons skilled in the art upon reference to the description. It is therefore intended that the appended claims encompass any such modifications or embodiments.

[0092] As will be recognized by those skilled in the art, the innovative concepts described in the present application can be modified and varied over a tremendous range of applications, and accordingly the scope of patented subject matter is not limited by any of the specific exemplary teachings given.

1. A motion tracking method for determining the location and orientation of at least one object moving in space, comprising the steps of:

- generating structured light;
- projecting structured light onto a target;
- receiving return light from the target through an optical receiver;
- converting the return light into coordinate data; and
- translating the coordinate data into motion information.

2. The method of claim 1, further comprising the step of adjusting an MRI scan to compensate for the motion information.

3. The method of claim 1, further comprising the step of placing the target inside an MRI machine.

4. The method of claim 1, further comprising the step of coordinating the target with a patient surface.

5. The method of claim 1, further comprising the step of originating the structured light source within the MRI apparatus.

6. The method of claim 1, further comprising the step of generating the structured light from a source selected from a group consisting of: a low-intensity pulsed light source, or continuous light source.

7. The method of claim 1 further comprising the step of sensitizing the optical receiver to at least one non-visible frequency.

8. The method of claim 2, further comprising the step of transmitting the motion information to a computer for alignment.

9. The method of claim 2, further comprising the step of guiding an interventional procedure with the motion information.

10. The method of claim 2, further comprising the step of evaluating changes in brain images with the motion information.

tion acquired over time periods selected from the group consisting of minutes, hours, days, weeks, and months, or a combination thereof.

11. A method for detecting position changes in movement during a medical imaging operation, comprising the steps of: generating a structured light coupled to a target; receiving the structured light through an optical receiver; converting the structured light into coordinate data; measuring an initial position of a patient with the structured light; measuring a second position of the patient with the structured light; determining a position shift between the initial position and second position; and transmitting the position shift to a medical imaging device.

12. The method of claim **11**, further comprising the step of adjusting the medical device to correct for the position shift.

13. The method of claim **11**, wherein the step of transmitting further comprises:

transmitting the position shift to an MRI device.

14. The method of claim **11**, wherein the step of generating structured light further comprises the steps of: providing a structured light projector; and, focusing the structured light projector on a patient.

15. The method of claim **11**, wherein the step of generating structured light further comprises:

attaching a reflective pattern to a patient; and irradiating the pattern with a coherent light source.

16. The method of claim **11**, wherein the step of receiving includes the step of pulling a CCD camera.

17. The method of claim **15**, wherein the step of receiving includes receiving at least two frequencies of light.

18. The method of claim **11**, wherein the step of generating includes the step of using a laser focused through a filter that acts as a structured light generator.

19. A method of analyzing movement of an object comprising the steps of:

receiving structured light from the object; and

analyzing the structured light to determine movement of the object.

* * * * *

Motion Tracking for Medical Imaging: A Nonvisible Structured Light Tracking Approach

Oline Vinter Olesen*, Rasmus R. Paulsen, Liselotte Højgaard, Bjarne Roed, and Rasmus Larsen

Abstract—We present a system for head motion tracking in 3D brain imaging. The system is based on facial surface reconstruction and tracking using a structured light (SL) scanning principle. The system is designed to fit into narrow 3D medical scanner geometries limiting the field of view. It is tested in a clinical setting on the high resolution research tomograph (HRRT), Siemens PET scanner with a head phantom and volunteers. The SL system is compared to a commercial optical tracking system, the Polaris Vicra system, from NDI based on translatory and rotary ground truth motions of the head phantom. The accuracy of the systems was similar, with root mean square (rms) errors of 0.09° for $\pm 20^\circ$ axial rotations, and rms errors of 0.24 mm for ± 25 mm translations. Tests were made using 1) a light emitting diode (LED) based miniaturized video projector, the Pico projector from Texas Instruments, and 2) a customized version of this projector replacing a visible light LED with a 850 nm near infrared LED. The latter system does not provide additional discomfort by visible light projection into the patient's eyes. The main advantage over existing head motion tracking devices, including the Polaris Vicra system, is that it is not necessary to place markers on the patient. This provides a simpler workflow and eliminates uncertainties related to marker attachment and stability. We show proof of concept of a marker less tracking system especially designed for clinical use with promising results.

Index Terms—Motion estimation, positron emission tomography, stereo image processing, stereo vision, structured light system.

I. INTRODUCTION

THE TOMOGRAPHIC reconstruction of 3D and time varying 3D medical images from a series of scanning modalities including X-ray, computed tomography (CT),

magnetic resonance imaging (MRI), and positron emission tomography (PET) requires sequential data recording over time. Patient motion during acquisition time will result in a lower image quality or even render the examination useless for PET imaging [1]. Our focus is on the Siemens High Resolution Research Tomograph (HRRT) PET scanner, which is a brain scanner with an isotropic spatial resolution of 1.4 mm [2]. Motion induced image degradation increases with increasing scanner resolution and thus head motion counteracts the technological advances of high resolution scanners. The probability of patient motion occurring increases with acquisition time. For structural or anatomical imagery, patient motion can sometimes be estimated and compensated directly from the scan recordings, e.g., in cardiac MRI [3] and lung CT [4]. For functional 3D scans such as PET and fMRI low contrast and spatially sparse events hampers the direct estimation of motion from the recordings themselves, and external motion detection and tracking is preferred [5]–[8]. An optical real time motion tracking system (Polaris System, Northern Digital Inc.) has been preferred for human studies [9]. An alternative optical tracker demonstrated on animals includes [10], [11]. These systems register 3–6 infrared retro reflecting markers fixed in a position relative to each other. They are either glued onto the animal directly or mounted onto a tracking tool and then fixed to the subject. For human head tracking different types of band-aid, helmets, wet-caps, or goggles have been implemented. In a clinical setting attaching markers is an additional element in a busy work flow, additional discomfort to the patient, and with some of the fixation solution listed above the markers are likely to move independently of the patient's head with head motion giving rise to erroneous motion estimates. Experience also shows that a marker based tracking system has problems registering the markers in the narrow scanner geometry and the accuracy of the system affects the motion correction results.

The purpose of our research is to develop a new 3D head tracking system that 1) does not need any markers, 2) fits to the narrow geometry of the Siemens HRRT PET scanner, 3) is comfortable for the patients, and 4) can potentially be built into future PET scanners. Instead of tracking a geometrical object attached to the patient's head we propose to track the face itself. The human face has a rich collection of texture and color variations including common features, e.g., eyes, eyebrows, mouth, lips, and person specific features, e.g., moles. However, as we want to infer brain motion we concentrate on geometrical features that are less variant to facial expression, e.g., nose tip, the bridge of the nose, and cheekbones. These features are almost featureless in color and texture space and are characterized by

Manuscript received June 17, 2011; revised August 02, 2011; accepted August 08, 2011. Date of publication August 18, 2011; date of current version December 30, 2011. This work was supported in part by Siemens Healthcare A/S and in part by The Danish Agency for Science, Technology, and Innovation. Asterisk indicates corresponding author.

*O. V. Olesen, is with the Department of Informatics and Mathematical Modelling, Technical University of Denmark, DK-2800 Lyngby, Denmark and also with Siemens Healthcare, DK-2750, Ballerup, Denmark, and also the Department of Clinical Physiology, Nuclear Medicine & PET, Rigshospitalet, Copenhagen University Hospital, University of Copenhagen, DK-2100 Copenhagen, Denmark (e-mail: <http://www.imm.dtu.dk/~ovol/contact.htm>).

R. R. Paulsen and R. Larsen are with the Department of Informatics and Mathematical Modelling, Technical University of Denmark, DK-2800 Lyngby, Denmark.

L. Højgaard is with the Department of Clinical Physiology, Nuclear Medicine & PET, Rigshospitalet, Copenhagen University Hospital, University of Copenhagen, DK-2100 Copenhagen, Denmark.

B. Roed is with Siemens Healthcare, DK-2750 Ballerup, Denmark.

Color versions of one or more of the figures in this paper are available online at <http://ieeexplore.ieee.org>.

Digital Object Identifier 10.1109/TMI.2011.2165157



Fig. 1. Photographs of a volunteer outside (top) and inside (bottom) the HRRT PET scanner with the SL system in the front mounted on the gantry.

their surface curvature and joint organization. A stereo vision system using structured light is an ideal way of recovering the surface of such color and texture less structures. By projecting a pattern onto the surface of interest we obtain surface features that when observed in a camera given proper geometrical calibration can be used to recover 3D surface point clouds. Different structured light patterns have been suggested including binary patterns, gray codes, phase shift gray scale patterns, stripe and grid indexing, and hybrid methods. [12] provides a comprehensive survey. A competitive technique providing a balance between the number of projections required and the complexity of the computations as well as providing subpixel resolution is the phase-shifting interferometry (PSI) method [13].

In order to track motion the recovered 3D point clouds must be aligned to a reference position. The limited system field-of-view (FOV) composed of: the camera projection FOV, facial geometry, and the size of rotation and translation will result in a limited overlap between the acquired point clouds. Thus, a resistant and robust iterative closest point (ICP) alignment to an initial precomputed template surface can be used to estimate rigid body motion of the head inside the scanner tunnel. The classical ICP algorithm [14] registers and aligns two point clouds with no prior correspondence. Several efficient variants of the ICP algorithm have been published [15].

In [16], we have shown first results using such a SL system based on projection of visible light patterns. In Fig. 1, this prototype system is shown mounted on the Siemens HRRT scanner with a volunteer outside and inside the scanner. For the purpose

of illustration the system is shown with the visible light projector such that the projected stripe pattern can be seen on the face of the volunteer. The system consists of a central video projector and two laterally placed cameras. The scanner imposes severe restrictions on the placement of cameras and projector and the subjects face is viewed at an oblique angle. While this system fulfills the requirements that it does not need markers, fits to the scanner geometry, and can potentially be built into future PET scanners it will also provide potential discomfort to the patient by shining light directly into the patients eyes.

In this system, the illuminated area is chosen to be large enough to cover relevant parts of the facial geometry and small enough to primarily illuminate the face. Restrictions are at the same time imposed by the scanner geometry. The result can be seen in Fig. 1. For large rotations and translations the overlap between the illuminated areas may be as low as 50%. Due to this partial overlap of point clouds a point rejection approach is applied with the ICP algorithm. Points matched to the border of the reference point cloud are rejected. This is nontrivial for raw point clouds. To overcome this, we represent our reference as a triangulated template surface computed using a state of the art surface reconstruction algorithm [17]. Compared to the popular Poisson surface reconstruction algorithm [18], the Markov random field surface reconstruction algorithm [17] deals particularly well with human body scans.

In this paper, we present a new NIR-SL system based on a near infrared (NIR) video projector realized by customization of a Texas Instruments Pico projector. The system fulfills the requirement of not providing additional discomfort to the patient. We will review the PSI method and the point cloud alignment. Moreover, we will provide quantitative evaluations of the performance of the SL and NIR-SL and compare these to the commercially available Polaris Vicra system. We demonstrate the system on a volunteer inside the HRRT PET scanner while not exposing the volunteer to any radioactivity.

II. SYSTEM REQUIREMENTS

The tracking system must satisfy a number of technical and clinical requirements. 1) The registration of the position must be estimated simultaneously so that a detected PET event known as a line of response (LOR) can be repositioned before the PET image reconstruction. 2) The tracking volume must cover the range of the possible head motion in the HRRT scanner. 3) The system must fit the narrow geometry of the PET scanner. 4) The accuracy of the tracking system has to be better than the spatial resolution of the PET scanner, otherwise the motion correction will increase the blurring instead of reducing it. 5) The system must not interfere with the PET acquisition. 6) The sample frequency has to be at least twice as high as the frequency of head motion to avoid aliasing, according to the Nyquist criterion. However, due to the relatively low count rate in PET, a tracking frequency of 5–10 Hz is adequate [9] or even less if applying the frame repositioning motion correction method [5]. The clinical requirements are at least as important as the technical requirements. To be a part of clinical routines the tracking system must be as follows. 1) Simple to use with a preference for a fully automated system. 2) The tracking system must have an easy interface with the PET scanner. 3) It must be robust and have a

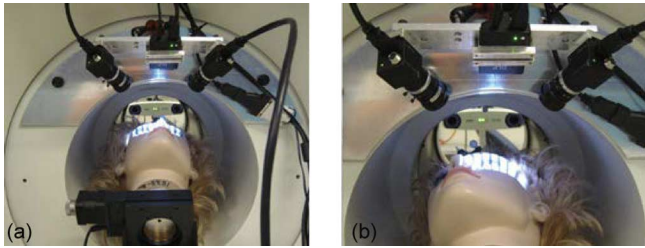


Fig. 2. Photographs of the mannequin head mounted to a rotary stage inside the HRRT PET scanner in two positions: (a) 0° and (b) -20° . The motor stage is seen in the bottom and the Polaris sensor in the back (the tracking tool can just be discerned above the forehead).

flexible design to be a part of the daily routine. 4) The system must be comfortable for the patients, since an uncomfortable patient will introduce motion which is counterproductive for both the patient's well being and the image quality. 5) Finally, the hygiene requirements of hospital use have to be met.

Commercial surface scanners are available. However, they are not compatible with high resolution PET brain scanners for the following reasons. They do not fit the narrow scanner geometry, are not fast enough as a tracking system, and do not use an invisible light source. A visible light source is uncomfortable for the patients and might introduce motion or at worst may interrupt the scanning.

III. MATERIALS AND METHODS

We intend to integrate a 3D surface scanner into the HRRT PET brain scanner and use it to track patient motion during the PET scans. At each tracking frame a partial 3D point cloud of the patient's head is processed in the tracker coordinate system and aligned to an initial template surface reconstruction referred to as the *reference target*.

A. Structured Light Tracking System

The SL system consists of a digital light processing (DLP) projector (DLP Pico Projector, Texas Instruments) with HVGA resolution (480×320) and two gray scale charge coupled device (CCD) cameras (Point Grey Research) with a resolution of 1288×964 . The SL system is designed to match the narrow scanner geometry of the HRRT PET scanner with a flexible design that is easy to mount on the scanner gantry. The SL system mounted on the gantry of the HRRT PET scanner is shown in Fig. 2 just above the patient tunnel. The image plane of the DLP projector consists of micro mirrors that are switched on and off to control every pixel of the projected image. This recent technology has improved the quality of the image projection and made it possible to achieve submillimeter accuracy of surface measurements [13]. The size of this digital micro mirror device (DMD) is $2.42 \text{ mm} \times 3.63 \text{ mm}$ and the size of the CCD chip is $3.60 \text{ mm} \times 4.80 \text{ mm}$. The cameras and projector are connected to a computer and synchronized through a custom software setup. Patterns are projected onto the patient's face and captured as images by the CCDs. The region of interest (ROI) is around the bridge of the nose, seen as the bright region in Fig. 1 bottom. This ROI is chosen due to limited facial motions at the bridge of the nose and because of the high surface curvatures. The system was optimized to have the camera positioned

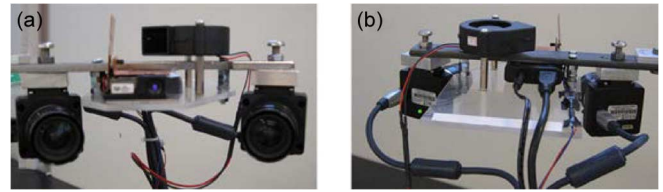


Fig. 3. NIR-SL system with a modified Pico DLP. In the top a cooling fan is directed at the LED fixed to a copper plate.

10–20 cm from the subject and the distance between the projector lens and the camera lens was 8.5 cm resulting in an angle of 30° between the image axis of the camera and the projector.

The SL system was modified with a NIR light emitting diode (LED) in order to meet the clinical requirements for such a system. The system has to be comfortable for the patients and shifting patterns of visible light projecting into the eyes of the patients is not acceptable during long acquisitions. A prototype of the NIR-SL system is seen in Fig. 3 with a specially designed DLP projector (DLP Pico Projector, modified). One of the original three LEDs was bypassed by a NIR LED connected to a separate power supply allowing for adjustment of the light intensity. The inserted LED was cooled by an external fan fixed to the system.

B. Tracking Experiments

1) *Phantom Study*: The performance of the tracking approach was evaluated by a set of experiments on the HRRT PET scanner with simultaneous tracking using the Polaris Vicra system. A mannequin head was placed inside the patient tunnel as seen in Fig. 2. It was mounted onto a nanorotary motor stage from Thorlabs. The stage made it possible to perform highly controllable rotations of the head. The stage was programmed to rotate in steps of 5° from -20° to 20° . The movements were repeated nine times. At each stationary position a set of four phase-shift images were captured with the SL systems. Furthermore, the phantom was translated in the axial direction in steps of 10 mm across six positions repeated four times. Axial translation is often seen when patients are moving their legs or relaxing neck and shoulders. The performed translation steps were measured with a sliding canvas with an estimated accuracy of $\pm 0.01 \text{ mm}$. At each experiment a 3D point cloud was reconstructed using PSI as described in Section III-D. This study extends the experiment described in [16].

We used the 0° position as the reference position and the pose of the head is estimated relative to this position. The alignment method has also been improved to handle greater motion compared to [16]. This was done by increasing the partial overlap between the reference target and the 3D point clouds at each tracking frame. The reference target was based on 3D point clouds captured outside the HRRT PET scanner just before the subject entered the scanner. Thus a larger region of the face surface was represented in the reference target compared to [16] where point clouds from the initial position inside the HRRT PET scanner were reconstructed and used as the reference target. The reference target was moved into the position at zero degrees before the pose estimation of the 3D point clouds. The Polaris Vicra tracking tool was fixed to the forehead of

the mannequin head as for patients to track the head motions during the PET acquisition [19]. While the Thorlabs stage provides baseline rotation data, the Polaris Vicra system recorded the motions of the head simultaneously with the image capturing of the SL system. Fig. 2 shows the set up of the experiments where the SL system is seen in the front and the Polaris sensor is seen in the back behind the patient tunnel. Fig. 2(a) shows the head in the reference position at 0° and Fig. 2(b) shows the most extreme rotation of the head to the left at -20° . The Polaris Vicra system directly provides a 3×3 rotation matrix \mathbf{R} (with elements R_{ij}) and a translation vector \mathbf{t} with respect to a reference position. The SL systems uses a software package Sumatra [20] for the ICP alignment returning \mathbf{R} and \mathbf{t} . To be able to compare the rigid motion estimates from the SL systems and the Polaris Vicra system with the baseline translations and baseline rotations provided by the Thorlabs stage, the rotation angle θ , direction of rotation axis \mathbf{v} , and a point on the line \mathbf{c} is determined from \mathbf{R} and \mathbf{t} [21]

$$\begin{aligned}\theta &= \arccos((\text{trace}(\mathbf{R}) - 1)/2) \\ \mathbf{v} &= \frac{1}{2 \sin(\theta)} [R_{32} - R_{23} \ R_{13} - R_{31} \ R_{21} - R_{12}]^T \\ \mathbf{c} &= (\mathbf{I} - \mathbf{R})^{-1} \mathbf{t}\end{aligned}\quad (1)$$

where \mathbf{I} is the identity matrix.

2) *Human Study*: We tested the system on a volunteer inside the HRRT PET scanner combined with the Polaris Vicra tracking. The volunteer was positioned as a patient would be and fixed using a vacuum bag as is normally done in the clinical routine at Rigshospitalet, Copenhagen. A reference target was obtained outside the HRRT PET scanner just before the subject entered the PET scanner. The reference target was constructed by aligning 3D point clouds recorded in four different SL system positions and reconstructing a triangulated surface representation. In this way the reference target has full coverage of the face. Inside the HRRT PET scanner the volunteer was asked to move the head into 14 different positions corresponding to movements often observed in PET brain imaging: 1) sidewise rotation, 2) upward rotation, and 3) axial translation. The registered motions are evaluated by comparing the angle of rotation relative to a mean position for each of the systems using (1). The mean rotation $\underline{\mathbf{R}}$ is determined as [22]

$$\begin{aligned}\underline{\mathbf{R}} &= \arg \min_{\mathbf{R}} \sum_i \theta^2(\mathbf{R}^{-1} \mathbf{R}_i) \\ &\approx \arg \min_{\mathbf{R}} \sum_i 3 - \text{trace}(\mathbf{R}^{-1} \mathbf{R}_i) \\ &= \arg \max_{\mathbf{R}} \sum_i \text{trace}(\mathbf{R}^{-1} \mathbf{R}_i) \\ &= \arg \max_{\mathbf{R}} \text{trace} \left(\mathbf{R}^{-1} \sum_i \mathbf{R}_i \right).\end{aligned}\quad (2)$$

The solution to (2) is found by singular value decomposition (SVD) $\sum_i \mathbf{R}_i = \mathbf{U} \mathbf{D} \mathbf{V}$. Introducing the matrix $\mathbf{S} = \text{diag}(1, 1, \det(\mathbf{U} \mathbf{V}))$ we have the mean rotation given as

$$\underline{\mathbf{R}} = \mathbf{U} \mathbf{S} \mathbf{V}.\quad (3)$$

C. Pose Estimation

We wanted to estimate the rigid body transformation from the current 3D scan to the reference scan. The scans are unstructured point clouds where approximate estimates of the point normals exist. We are using a specialized version of the ICP algorithm [14]. Initially, two surfaces for each camera respectively are created based on 2–4 scan positions. Both cameras produce a 3D point cloud representation of the part of the head in its FOV. Scans for each camera are aligned and merged to create a reference target that covers the FOV of each camera using the method described in [20]. In this method the surfaces are created using the Markov random field surface reconstruction algorithm [17]. It is based on an implicit description of the surface combined with a regularization step that makes it well suited for human body scans. Since the surface reconstruction algorithm by default computes surfaces that extend beyond the point cloud, a postprocessing step is needed where the surface is cropped to fit the point cloud. This is done by removing parts of the surface that are not supported by reliable input points. Support is defined as being within a distance d of an input point, where d is estimated as the average neighbor distance in the input point cloud. The result is a polygonised surface patch, where the edge vertices are defined as having only one adjacent triangle. For each point in the current scan, the closest point on the triangulated surface is found using a k D-tree based approach. If the point falls on an edge vertex, the point match is discarded. The remaining point matches are used to compute the rigid body transformation using the solution found in [21]. Using this method the transformation bringing the current scan into alignment with the reference surface is computed. Prior to the alignment noisy points, non connected points, and small isolated clusters of points were excluded from the point cloud, following the approach from [17]. The alignment of the partial face surfaces into the reference target is computed twice. In the first round, the point clouds are aligned to a target representing most of the face to generate a robust prealignment. In the second alignment round the target is reduced to include the stable part of the face reconstruction just around the nose bridge.

D. 3D Point Cloud Generation

We use PSI to determine the correspondence between the two image planes; the projector image plane (u_p, v_p) and the image plane of one of the cameras (u_c, v_c) (see Fig. 4). From a series of three captured interferograms (2D images) the wave front phase is computed and converted to line positions on the projector image plane [23]. Thus, a given phase of cosine patterns $I_k(u_p, v_p)$ on the captured images $cI_k(u_c, v_c)$ correspond to a position on the projector image plane after phase unwrapping. The cosine patterns are generated by

$$\begin{aligned}I_k(u_p, v_p) &= a \left(1 + \cos \left(\frac{2\pi}{p} u_p + s_k \right) \right) + b \\ s_k &= \frac{2\pi}{3} (k - 2) \quad \text{and} \quad k = 1, 2, 3\end{aligned}$$

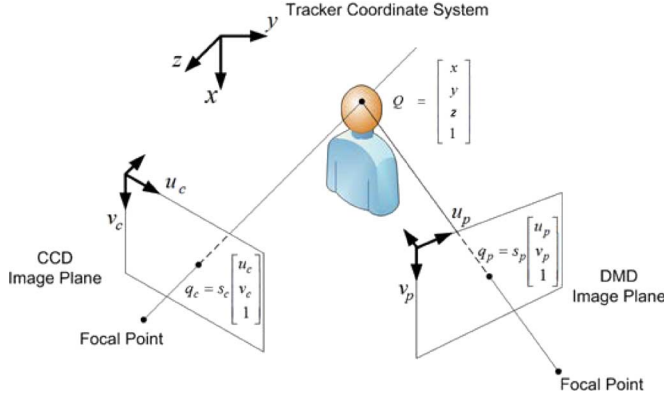


Fig. 4. Sketch of the relation between the world coordinate system (x, y, z) and the image planes for one camera (u_c, v_c) and the projector (u_p, v_p) . Q is a point in the tracker coordinate system and q_c and q_p are points in the CCD image plane and the DMD image plane, respectively.

where a is the amplitude, b is the bias, s_k is the shift, and k is the pattern number of the cosine function. This results in the three captured interferograms

$$cI_k(u_c, v_c) = I_{av} + I_{mod} \cos(\phi(u_c, v_c) + s_k)$$

with the three unknowns; the phase $\phi(u_c, v_c)$, the average of the intensity I_{av} , and the modulation of the intensity I_{mod} . Solving the above equation gives the phase

$$\phi(u_c, v_c) = \arctan \left(\sqrt{3} \frac{cI_1(u_c, v_c) - cI_3(u_c, v_c)}{2cI_2(u_c, v_c) - cI_1(u_c, v_c) - cI_3(u_c, v_c)} \right).$$

Since the phase is periodic, the phase has to be unwrapped to achieve a continuous phase image. Several methods to perform phase unwrapping exist. Experiments showed that the method described in [24] performs well with our data. This method is a 2D path-independent algorithm where the image is divided into regions based on the 2π phase jumps. The points on the image planes are converted into 3D coordinates using a simple pinhole model for both the cameras and the projector and assuming the calibrations parameters for all three components are known. The calibration matrices of the cameras \mathbf{P}_{c1} and \mathbf{P}_{c2} and the projector \mathbf{P}_p are 3×4 matrices and from the perspective camera model we have for one camera

$$q_c = \mathbf{P}_c Q$$

or

$$s[u_c \ v_c \ 1]^T = \mathbf{P}_c [X \ Y \ Z \ 1]^T.$$

This can be combined into

$$u_c = \frac{\mathbf{P}_c(1)Q}{\mathbf{P}_c(3)Q} \quad \text{and} \quad v_c = \frac{\mathbf{P}_c(2)Q}{\mathbf{P}_c(3)Q}$$

where the number of the calibration matrix represents a row e.g., $\mathbf{P}_c(3)$ is the third row of \mathbf{P}_c . Similar equations are valid for the projector. A new set of equations can be set up and solved with respect to coordinates in the tracker coordinate system. The

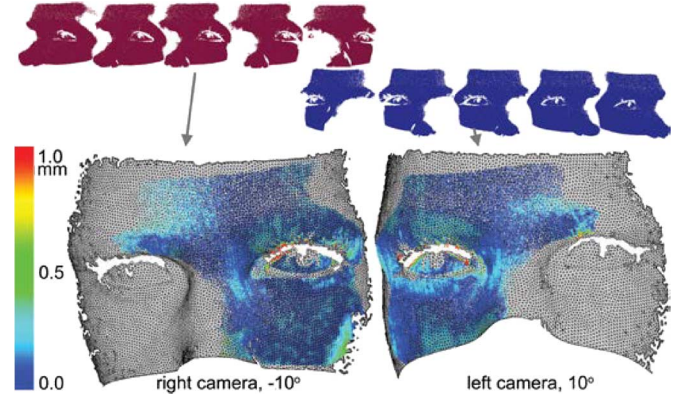


Fig. 5. Results of the mannequin head experiment. Top: 3D point clouds at the nine positions. Left to right from -20° to 20° . Blue images represent the left camera and red images represent the right camera. Bottom: ICP alignment at two positions $\pm 10^\circ$. Alignments into the reference target are shown on top of the reference surfaces. The colors represent the errors [mm] as the distance to target.

coordinates in the CCD image plane and the vertical coordinate of the DMD

$$u_c \cdot \mathbf{P}_c(3) - \mathbf{P}_c(1) \cdot Q = 0$$

$$v_c \cdot \mathbf{P}_c(3) - \mathbf{P}_c(2) \cdot Q = 0$$

$$u_p \cdot \mathbf{P}_p(3) - \mathbf{P}_p(1) \cdot Q = 0.$$

The new set of linear equations yields a 3D point in the tracker coordinate system

$$s[X \ Y \ Z]^T = \mathbf{A}^{-1}\mathbf{b}$$

where \mathbf{A} is a matrix and \mathbf{b} is a vector consisting of calibration parameters. Further details of the system calibration and 3D coordinate computations can be found in [25].

IV. EXPERIMENTAL RESULTS

Fig. 5 (top) shows the 3D point clouds at the nine different positions from -20° to 20° (left to right) for one of the nine experiments with the mannequin head. The red and the blue point clouds represent the right and left camera, respectively. As seen, the point clouds are highly detailed with little noise and outliers, demonstrating the high spatial resolution of the system. The right camera has a more favorable angular position with respect to the surface for the negative rotations, and the left camera for the positive rotations. Thus, we have used point clouds for the camera with the largest angle between the image axis and the surface as shown on Fig. 5. The point clouds are aligned into the reference target and two results of the ICP alignment are shown in Fig. 5 (bottom) at $\pm 10^\circ$ from the right and left camera, respectively. In Fig. 5 (bottom), the color coding of the aligned scans represents the individual per-point alignment error. It is computed as the distance from the point to the closest point on the reference target seen in the back. The errors between the reference target and the aligned points are in the order of 0–0.2 mm with the largest errors around the eyes. The medians of the point errors in Fig. 5(bottom) are 0.10 mm and 0.09 mm. As previously mentioned, the motion of the Thorlabs stage is considered the ground truth motion. The errors of the estimated motion are plotted as a function of the ground truth motion in

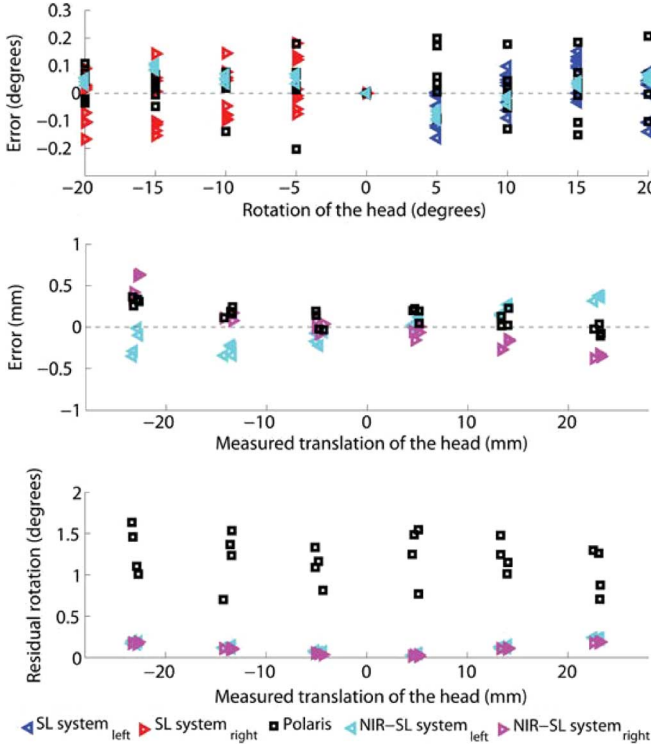


Fig. 6. Comparison of the SL system, NIR-SL system, and the Polaris Vicra system; Rotation study: (top) differences between the estimated and the performed rotations as a function of the performed rotation. Polaris Vicra rotation experiment 3 has errors $> 0.5^\circ$ and not represented in the plot. Translation study: (middle) differences between the estimated and the performed translations as a function of the performed translation; (bottom) the estimated absolute rotations that ideally should be 0° for the translation study.

Fig. 6. In Fig. 6 (top) the results from variation in the rotation is shown. The blue and red points represent estimates from the SL system's left and right camera, respectively. The black points are the simultaneously captured results from the Polaris Vicra system.

The errors of the SL system are less than 0.2° from the performed rotation when using the right camera (red) for negative rotations and the left camera (blue) for the positive rotation with a rms error of 0.089° . This is a similar result as the Polaris Vicra system, which has a rms error of 0.086° . One of the Polaris Vicra tracking (experiment no. 3) is treated as an outlier and not included in the rms error. We can not operate the NIR-SL system simultaneously with the Polaris Vicra system since both systems used light at 850 nm and would influence each others estimates. The NIR-SL systems has been used for the same experiment in a second run and the resulting errors are plotted in light blue. The NIR-SL system has a rms of 0.061° .

In Fig. 6 (middle) the results from varying the translation is shown. Here we compare the NIR-SL system to the Polaris Vicra system. Again the experiment is done in two runs, one for the NIR-SL system, and one for the Polaris Vicra system in order to avoid interference. The light blue and magenta points represent estimates from the NIR-SL systems left and right camera, respectively. The black points are the results from the Polaris Vicra system. The rms for NIR-SL (left) is 0.24 mm, for NIR-SL (right) is 0.28 mm, and for Polaris 0.18 mm. In Fig. 6 (bottom)

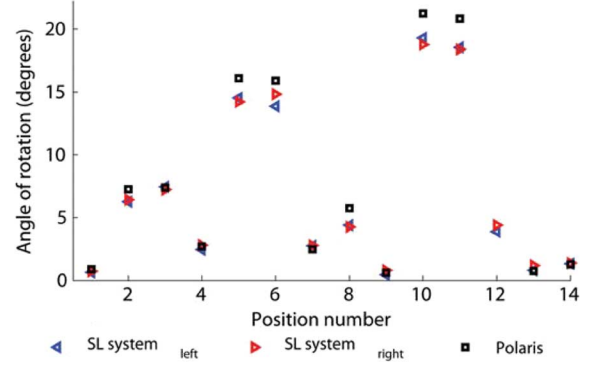


Fig. 7. Comparison of the left SL system, the right SL system, and the Polaris Vicra system on a human test subject ; the estimated relative rotation to a mean rotation for 14 positions. No Polaris data for pose 12 due to too few markers registered by the Polaris sensor.

the estimated absolute rotations for the translation study are shown. These should ideally be 0° . The light blue and magenta points represent estimates from the NIR-SL systems left and right camera, respectively. The black points are the results from the Polaris Vicra system. The NIR-SL system deviations are below 0.2° . The Polaris Vicra ranges up to 1.7° . The large deviation for the Polaris may be ascribed to the longer distance between the sensor and the object for this system.

Furthermore, we have tested the SL system on a volunteer in the HRRT PET scanner. The purpose is to demonstrate the clinical usability of the system. The position of the volunteer was registered in 14 poses and estimated relative to the mean position. The subject had translated 5–43 mm and rotated 1° to 21° compared to the mean position. Fig. 7 shows the results of the relative rotation in the 14 recorded head poses and compares the three systems: the left SL system, the right SL system, and the Polaris Vicra system. The standard deviation (SD) between the differences of the systems are: 1) $SD(Pol - SL_{left}) = 0.85^\circ$, 2) $SD(Pol - SL_{right}) = 0.97^\circ$, and 3) $SD(SL_{left} - SL_{right}) = 0.41^\circ$. It is seen that the difference between the systems increases with the angle of rotation from the centre, cf. Fig. 7.

Fig. 8 shows the 3D point clouds before (left) and after (right) the ICP alignment to the reference target for two head poses. These are pose 7 and pose 10 which are close to the head poses shown in Fig. 1. These poses are moved approximately 8 mm and 3° for pose 7 and 35 mm and 19° for pose 10 compared to the reference position. As seen in Fig. 8, parts of the unaligned point clouds (left) are missing from the aligned point clouds (right). These parts are excluded either due to detected errors or simply due to occlusion and shadowing. The mean of the median values of these point errors is 0.19 mm ($\pm SD = 0.02$ mm) for the two poses shown in Fig. 8(right). It is noted that the per point errors for the two poses are similar even though pose 10 is one of the outlying poses. Finally, we demonstrate that the NIR illumination has the same performance for surface registration as visual light illumination. Fig. 9 shows results of the NIR-SL system for a human volunteer. This experiment was conducted outside the HRRT PET scanner with the volunteer sitting upright in a chair with support for the back and not for the head. The centroids of the reconstructed 3D point clouds from the four positions were 31–46 mm from the centroid of the

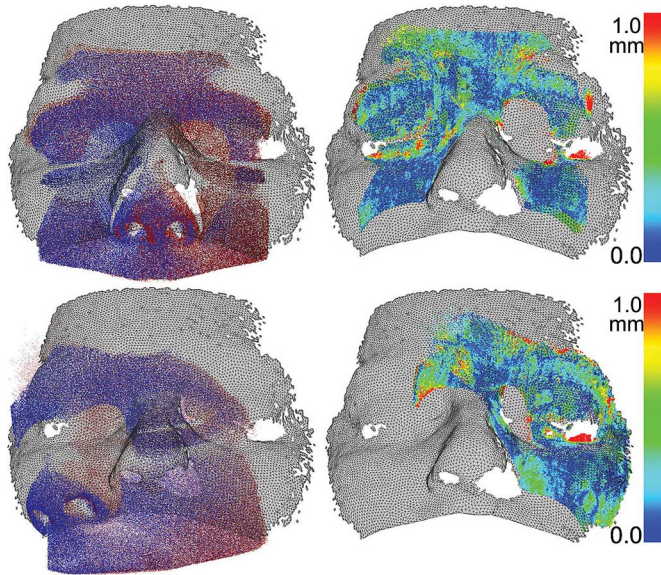


Fig. 8. Human surface scans inside the HRRT PET scanner in pose 7 and pose 10. These poses almost correspond to the positions shown in Fig. 1. 3D point clouds before (left images) and after (right images) the ICP alignment of the left (blue) and right (red) system. The colors on the right images represent the distance [mm] to the target.

reference target. The main motions were axial/downward translation and sidewise rotation which are typical motions seen in PET brain imaging. The captured images are nonblurred and have high contrast (utilizing approximately 80% of the 8 bit colors). This supports the high quality of the captured images using the NIR LED. The reconstructed 3D point clouds correspond to the regions of the scanned surface. The errors of the ICP alignment are less than 0.5 mm for the majority of regions. The mean of the median values of these point errors are 0.29 mm (\pm SD = 0.09 mm) (compared to 0.19 mm (\pm SD = 0.02 mm) for the visual light illumination). Small areas especially at the borders and the nose have errors >1 mm seen as the red areas (Fig. 9).

V. DISCUSSION

A structured light system developed to register 3D head motion was applied to a clinical setting and shown to work given narrow scanner geometries such as the HRRT PET scanner. The design is miniaturized, flexible, and does not need any markers. These qualities make the system usable and valuable in a clinical setting. A markerless system is also timesaving and hygienic in terms of hospital use. Another important advance of not using markers is the elimination of the major source of error when attaching markers onto the head. When using the Polaris Vicra system there is potential risk that the tracking tool moves relative to the skull either because of the attachment or movements not related to the skull such as facial movements. Facial movements can obviously also introduce tracking errors with the SL system. However, this system relies on thousands of points thereby improving the robustness of the transformation estimation.

The structured light system was realized in both visible and NIR versions, SL and NIR-SL, respectively. The two systems were compared to the Polaris Vicra system on a phantom set up

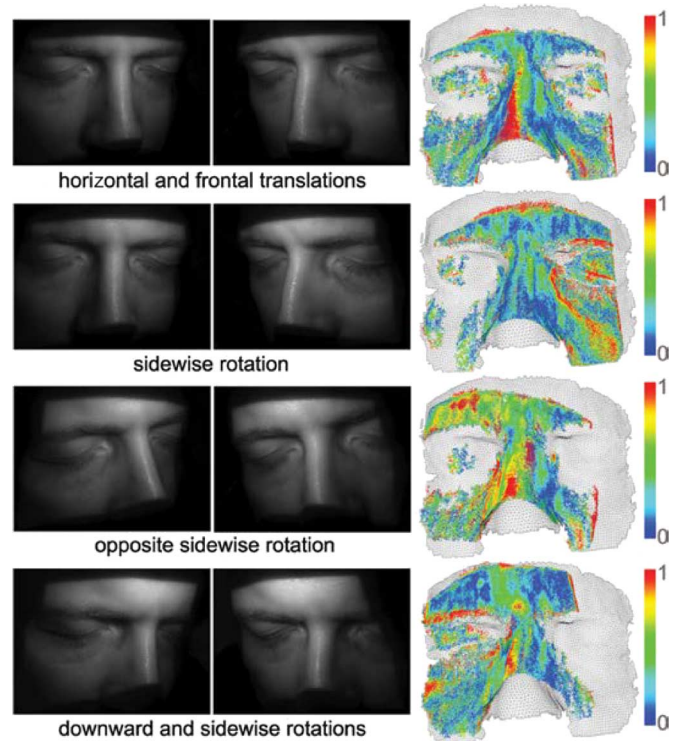


Fig. 9. NIR-SL results. Left: Captured regions with the two cameras. Right: Errors [mm] of the alignment on top of the triangulated reference target.

in order to get ground truth motions. The accuracy of the SL system was equal to the Polaris Vicra system with a rms error of 0.09° for axial rotation from -20° to 20° and a rms error of 0.26 mm for translation over a range of 50 mm (Fig. 6).

This result is supported by the accuracy found in [16] for a similar experiment. Thus, on a rigid object where the tool is fixed the accuracy of both systems are in the order of a few tenths of a millimeter for the brain region, e.g., if a head is rotating around the point of contact in the back head the displacement of the frontal brain lobe 10 cm away for a 0.09° rotation is $\tan(0.09^\circ) \cdot 10 \text{ cm} = 0.16 \text{ mm}$.

We believe this accuracy is representative of the achievable accuracy on humans since some aspects can be improved such as facial movements, time of image capturing, and combining the left and right systems as explained below. The accuracy are an order of magnitude less than the current resolution of the HRRT PET scanner.

A human volunteer study was performed inside the HRRT PET scanner to demonstrate the SL and NIR-SL systems usability for the HRRT PET scanner on humans. We have shown detailed 3D point clouds of the face surfaces which are aligned to the target with a median of the per point error of around 0.2 mm (Fig. 8). These errors are due to reflectance of the light, noise, and motion. The output transformations from the SL system are based on thousands of points and thus the accuracy of the rigid body transformation is expected to be $\ll 1 \text{ mm}$. From the comparison of the systems in 14 head poses we find twice as good agreement between the two SL systems ($\text{SD}(\text{SL}_{\text{left}} - \text{SL}_{\text{right}}) = 0.41^\circ$) compared to the agreement between the Polaris Vicra system and one of the SL systems ($\text{SD}(\text{Pol} - \text{SL}_{\text{left}}) = 0.85^\circ$ and $\text{SD}(\text{Pol} - \text{SL}_{\text{right}}) = 0.97^\circ$).

Some poses have significant larger difference with the Polaris Vicra system (Fig. 7) for which we have no unique explanation. It could be due to the calibration of the SL system or motion of the Polaris tracking tool. We observed that the per point alignment error (Fig. 8) was not related to the size of the performed motion. The difference between the left and right SL system is at the same level as for the phantom experiment if we do not only consider the system with the best angular position relative to the surface. Therefore, the accuracy of a total SL system is improved by combining information from the left and right system taking the angular distortion into account or simply excluding point clouds with normals perpendicular to the image axis.

We have presented a miniaturized NIR-SL system for 3D head tracking. In this system, the visible LED of the original Texas Instruments Pico DLP was replaced with a NIR LED. We demonstrated the system on a human volunteer for four different head poses. The 3D point clouds are highly detailed as for the visible system. The median of the aligned per point errors is 50% larger than for the human volunteer study with the visible SL system. This could be explained by the differences between the experiments. In the NIR-SL case, the volunteer was sitting in a chair without head support, whereas for the SL case the volunteer was lying in the HRRT PET scanner with head support. This set up might have introduced some motion during the image capturing of a set of images of 3–4 s. The rate of the image capturing has not been optimized for these prototypes of the SL system.

Based on the detailed point clouds, the results of the aligned point clouds, and comparing the quality of the captured images we expect to obtain the same accuracy of this system compared to the visible SL system. The results with the NIR-SL system are representative for the experiments we have performed inside the HRRT PET scanner. This error indicates that the system will be able to accurately determine the pose changes for real humans in a clinical environment with simultaneous PET acquisition. In order to realize motion compensated HRRT PET imaging based on the NIR-SL system time synchronization between the HRRT PET scanner and the NIR-SL must be established, the HRRT PET and NIR-SL coordinate system must be aligned, the NIR-SL must be configured to run continuously, and an algorithm for motion compensated reconstruction must be in place. Basically, two approaches can be taken for motion compensation depending on the nature of the motions of the study subjects. The multiple acquisition frames method assumes that the subject lies still for longer periods of time interrupted by short periods of motion [5]. The motion tracking device is used to identify these periods of no motion. For each such period a PET image (frame) is reconstructed using standard algorithm. The frames are then combined to a reconstructed PET image in a second step. An alternative method does not make an assumption of the motion pattern but requires continuous estimates of pose [26]. In this case each PET event (LOR) is repositioned before using a standard reconstruction method.

VI. CONCLUSION

We present a compact vision system based on a customized Texas Instruments Pico DLP projector fitted with a NIR LED.

The system is adapted for motion correction in high resolution PET brain imaging. While the system's accuracy is comparable with the current state of the art optical trackers, it is more flexible and the system is fully automatic and does not rely on markers. Furthermore, the NIR LED ensures a more comfortable experience for the patients. This is a step toward a fully automatic tracking system designed for the HRRT PET brain scanner, but with potential use in other scanners and imaging modalities where an external tracking system is currently needed.

ACKNOWLEDGMENT

The authors would also like to thank Rigshospitalet for making clinical scanner facilities available. They would like to thank The John and Birthe Meyer Foundation for the generous donation of the HRRT PET scanner. Finally, they would like to thank the staff at The Mechanical Workshop at Rigshospitalet who helped them produce the mechanical devices.

REFERENCES

- [1] M. V. Green, J. Seidel, S. D. Steina, T. E. Tedder, K. M. Kempner, and C. Kertzman, "Head movement in normal subjects during simulated PET brain imaging with and without head restraint," *J. Nucl. Med.*, vol. 35, no. 9, pp. 1538–1546, 1994.
- [2] O. V. Olesen, M. Sibomana, S. H. Keller, F. Andersen, J. A. Jensen, S. Holm, C. Svarer, and L. Højgaard, "Spatial resolution of the HRRT PET scanner using 3D-OSEM PSF reconstruction," in *Proc. IEEE Nucl. Sci. Symp. Med. Imag. Conf.*, 2009, vol. M13-225, pp. 3789–3790.
- [3] M. B. Stegmann and H. B. W. Larsson, "Motion-compensation of cardiac perfusion MRI using a statistical texture ensemble," in *Proc. Functional Imag. Model. Heart*, 2003.
- [4] J. Ehrhardt, R. Werner, T. Frenzel, D. Säring, W. Lu, D. Low, and H. Handels, "Reconstruction of 4D-CT data sets acquired during free breathing for the analysis of respiratory motion," in *Proc. SPIE Med. Imag.*, 2006, vol. 6144, pp. 614414-1–614414-8.
- [5] Y. Picard and C. J. Thompson, "Motion correction of PET images using multiple acquisition frames," *IEEE Trans. Med. Imag.*, vol. 16, no. 2, pp. 137–144, Apr. 1997.
- [6] S.-K. Woo, H. Watabe, Y. Choi, K. M. Kim, C. C. Park, and P. M. Bloomfield, "Sinogram-based motion correction of PET images using optical motion tracking system and list-mode data acquisition," *IEEE Trans. Nucl. Sci.*, vol. 51, no. 3, pp. 782–788, Jun. 2004.
- [7] A. Rahmim, K. Dinelle, J. C. Cheng, M. A. Shilov, W. P. Segars, S. C. Lidstone, S. Blinder, O. G. Rousset, H. Vajihollahi, B. Tsui, D. F. Wong, and V. Sossi, "Accurate event-driven motion compensation in high-resolution PET incorporating scattered and random events," *IEEE Trans. Med. Imag.*, vol. 27, no. 8, pp. 1018–1033, Aug. 2008.
- [8] N. Raghunath, T. L. Faber, S. Suryanarayanan, and J. R. Votaw, "Motion correction of pet brain images through deconvolution: II. Practical implementation and algorithm optimization," *Phys. Med. Biol.*, vol. 54, no. 3, p. 813, 2009.
- [9] B. J. Lopresti, A. Russo, W. F. Jones, T. Fisher, D. G. Crouch, and D. E. Altenburger, "Implementation and performance of an optical motion tracking system for high resolution brain PET imaging," *IEEE Trans. Nucl. Sci.*, vol. 46, no. 6, pp. 2059–2067, Dec. 1999.
- [10] A. Weisenberger, S. Gleason, J. Goddard, B. Kross, S. Majewski, S. Meikle, M. Paulus, M. Pomper, V. Popov, and M. Smith *et al.*, "A restraint-free small animal SPECT imaging system with motion tracking," *IEEE Trans. Nucl. Sci.*, vol. 52, no. 3, pp. 638–644, Jun. 2005.
- [11] J. Goddard, S. Gleason, M. Paulus, R. Kerekes, S. Majewski, V. Popov, M. Smith, A. Weisenberger, B. Welch, and R. Wojcik, "Pose measurement and tracking system for motion-correction of unrestrained small animal PET/SPECT imaging," in *IEEE Nucl. Sci. Symp. Conf. Rec.*, 2003, vol. 3, pp. 1824–1827.
- [12] J. Geng, "Structured-light 3d surface imaging: A tutorial," *Adv. Opt. Photon.*, vol. 3, no. 2, pp. 128–160, 2011.
- [13] G. Frankowski and R. Hainich, "DLP-based 3D metrology by structured light or projected fringe technology for life sciences and industrial metrology," in *Proc. SPIE*, 2009, vol. 7210, p. 72 100C.

- [14] P. J. Besl and N. McKay, "A method of registration of 3D shapes," *IEEE Trans. Pattern Anal. Mach. Intell.*, vol. 14, no. 2, pp. 239–256, 1992.
- [15] S. Rusinkiewicz and M. Levoy, "Efficient variants of the ICP algorithm," in *Proc. Int. Conf. 3-D Digital Imag. Model.*, 2001, pp. 145–152.
- [16] O. V. Olesen, R. R. Paulsen, L. Højgaard, B. Roed, and R. Larsen, "Motion tracking in narrow spaces: A structured light approach," in *Medical Image Computing and Computer-Assisted Intervention—MICCAI 2010*, ser. Lecture Notes in Computer Science, T. Jiang, N. Navab, J. P. Pluim, and M. A. Viergever, Eds. New York: Springer, 2010, vol. 6363, pp. 253–260.
- [17] R. R. Paulsen, J. A. Bærentzen, and R. Larsen, "Markov random field surface reconstruction," *IEEE Trans. Visualizat. Comput. Graph.*, vol. 16, no. 4, pp. 636–646, Jul./Aug. 2010.
- [18] M. Kazhdan, M. Bolitho, and H. Hoppe, "Poisson surface reconstruction," in *Proc. Symp. Geometry Process.*, 2006, pp. 61–70.
- [19] O. V. Olesen, S. H. Keller, M. Sibomana, R. Larsen, B. Roed, and L. Højgaard, "Automatic thresholding for frame-repositioning using external tracking in PET brain imaging," in *Proc. IEEE Nucl. Sci. Symp. Med. Imag. Conf.*, 2010, p. M13-312.
- [20] R. R. Paulsen and R. Larsen, "Anatomically plausible surface alignment and reconstruction," in *Proc. Theory Practice Comput. Graph.*, 2010, pp. 249–254.
- [21] B. K. P. Horn, "Closed form solution of absolute orientation using unit quaternions," *J. Opt. Soc. A*, vol. 4, no. 4, pp. 629–642, 1987.
- [22] C. Gramkow, "On averaging rotations," *J. Math. Imag. Vis.*, vol. 15, no. 1, pp. 7–16, 2001.
- [23] P. Huang, Q. Hu, F. Jin, and F. Chiang, "Color-encoded digital fringe projection technique for high-speed three-dimensional surface contouring," *Opt. Eng.*, vol. 38, p. 1065, 1999.
- [24] M. Herráez, D. Burton, M. Lalor, and M. Gdeisat, "Fast two-dimensional phase-unwrapping algorithm based on sorting by reliability following a noncontinuous path," *Appl. Opt.*, vol. 41, pp. 7437–7444, 2002.
- [25] O. V. Olesen, M. R. Jørgensen, R. R. Paulsen, L. Højgaard, B. Roed, and R. Larsen, "Structured light 3D tracking system for measuring motions in PET brain imaging," in *Proc. SPIE Med. Imag.*, 2010, vol. 7625, p. 76250X.
- [26] R. Carson, W. Barker, J. Liow, and C. Johnson, "Design of a motion-compensation OSEM list-mode algorithm for resolution-recovery reconstruction for the HRRT," in *IEEE Nucl. Sci. Symp. Conf. Rec.*, 2003, vol. 5, pp. 3281–3285.